Mechanisms of shear band formation in heterogeneous materials under compression: The role of pre-existing mechanical flaws

Manaska Mukhopadhyay[1], Arnab Roy[1], and Nibir Mandal[1]

[1]Jadavpur University

November 24, 2022

Abstract

Using plane-strain compression experiments this article elucidates the competing mechanisms of shear band formation (spatially distributed narrow, sharp shear bands: NBs versus localized composite shear bands: CBs) in heterogeneous elastoplastic solids as a function of pre-existing weak flaws. Homogeneous representative models without pre-existing flaws produced uniformly distributed, closely spaced NBs in conjugate sets, symmetrically oriented at angles of 41°-44° to the compression axis. Heterogeneous models, in contrast, formed CBs at an angle of 46°-49°, localized preferentially against the flaws, leaving the host almost free from any band growth. With increasing finite strains (6% to 18%) the CBs grew to a characteristic wide-band structure, typically comprising a core of densely packed band-parallel sharp secondary bands, flanked by linear regions (transition zone) of closely spaced, across-band NBs. We provide a band density analysis to show the distinctive shear-band characteristics for the homogeneous and heterogeneous models. This study also investigates the effects of global strain-rate (ε') on the band localization mechanism in heterogeneous solids. Decreasing ε' (3 x 10-5 sec-1 to 2 x 10-5 sec-1) is found to transform the composite bands into well-defined homogeneous shear bands (HBs) that contain a homogeneously sheared core, flanked by narrow zones of gradational shear into completely unstrained walls. We support our experimental findings with numerical model simulations in the framework of visco-elasto-plastic rheology. The article finally presents a set of geological examples to discuss various types of shear band structures in the light of heterogeneous model findings.

Mechanisms of shear band formation in heterogeneous materials under compression: The role of pre-existing mechanical flaws

Manaska Mukhopadhyay, Arnab Roy and Nibir Mandal*

High Pressure and Temperature Laboratory, Department of Geological Sciences, Jadavpur University, Kolkata 700032, India.

Abstract

Using plane-strain compression experiments this article elucidates the competing mechanisms of shear band formation (spatially distributed narrow, sharp shear bands: NBs versus localized composite shear bands: CBs) in heterogeneous elastoplastic solids as a function of pre-existing weak flaws. Homogeneous representative models without pre-existing flaws produced uniformly distributed, closely spaced NBs in conjugate sets, symmetrically oriented at angles of 41°-44° to the compression axis. Heterogeneous models, in contrast, formed CBs at an angle of 46°-49°, localized preferentially against the flaws, leaving the host almost free from any band growth. With increasing finite strains (6% to 18%) the CBs grew to a characteristic wide-band structure, typically comprising a core of densely packed band-parallel sharp secondary bands, flanked by linear regions (transition zone) of closely spaced, across-band NBs. We provide a band density analysis to show the distinctive shear-band characteristics for the homogeneous and heterogeneous models. This study also investigates the effects of global strain-rate ($\dot{\varepsilon}$) on the band localization mechanism in heterogeneous solids. Decreasing $\dot{\varepsilon}$ (3×10^{-5} sec^{-1} to 2×10^{-5} sec^{-1}) is found to transform the composite bands into well-defined homogeneous shear bands (HBs) that contain a homogeneously sheared core, flanked by narrow zones of gradational shear into completely unstrained walls. We support our experimental findings with numerical model simulations in the framework of visco-elasto-plastic rheology. The article finally presents a set of geological examples to discuss various types of shear band structures in the light of heterogeneous model findings.

Keywords: shear band growth, polymer models, compression test experiments, mechanical heterogeneity, finite element modelling, visco-elasto-plastic rheology

1. Introduction

The shear failure mechanics is crucial to understand a wide spectrum of geodynamic phenomena, ranging from crustal scale tectonic deformation localization to earthquake dynamics. According to the classical theories, deforming elastic solids under increasing stresses attain a critical state, marked by a sharp jump in the displacement gradient across specific surfaces (strain localization) to undergo failure in the form of shear bands (Anand & Spitzig, 1980, 1982; Hutchinson & Tvergaard, 1980; Rice, 1976; Rudnicki, 1977; Rudnicki & Rice, 1975; Tvergaard et al., 1981). Such band structures generally occur as narrow, linear regions on a wide range of scales (a few microns to hundreds of kilometers) and accommodate large plastic creeps to form high-strain zones in Earth's lithosphere (Mancktelow & Pennacchioni, 2005; Meyer et al., 2017; Rogowitz et al., 2016; Scholz & Choi, 2021; Snyder & Kjarsgaard, 2013; Vauchez et al., 2012). A direction of recent studies focuses upon the growth mechanisms of deformation bands, primarily to address a number of key rock physics issues, such as composite structures of fault damage zones (Mitchell & Faulkner, 2009), porosity enhancement versus reduction in deformation bands (H. Fossen, 2010), and localized melt or fluid transport pathways (B. K. Holtzman, Groebner, et al., 2003; Benjamin K. Holtzman et al., 2005; R. F. Katz et al., 2006). A significant part of their insights has come from laboratory experiments (Bowden & Raha, 1970; Camwell & Hull, 1973; Nizolek et al., 2021; Reber et al., 2020; Sagapuram et al., 2018; Zielinski & Ast, 1983). For example, Bowden and Raha's experiments with polymer materials, e.g., polystyrene (PS) and polymethyl methacrylate (PMMA) recognize temperature (T) and strain rates ($\dot{\varepsilon}$) as principal physical factors to determine the mode of shear band localization in elasto-plastic solids under compression. At room temperature (T = 21°C) their PS experiments produced numerous sharp micro shear bands of ~1μm thickness, replaced by relatively wide, diffused shear bands at increasing temperature (T = 70°C) or reducing strain rates ($\dot{\varepsilon}$: 6 x 10^{-3}

56 sec^{-1} to 4 x 10^{-3} sec^{-1}). The other polymer showed a similar transition in the mode of shear band
57 localization as a function of T and $\dot{\varepsilon}$. A range of various practical materials, e.g., steel and rocks
58 have also been used to study their failure behavior under laboratory conditions (Anand &
59 Spitzig, 1980; David L. Kohlstedt & Holtzman, 2009). The shear band mechanisms in geological
60 conditions are found to be intricately complex due to various factors, such as syn-shearing
61 rheological transformations, fluid-assisted mineralogical changes, and long-time scale growth
62 with changing ambient conditions (Bauer et al., 2018; Condit & Mahan, 2018; Haakon Fossen &
63 Cavalcante, 2017; Putnis, 2021). To tackle such complexities, geoscientists have used numerical
64 models to understand the evolution of shear localization on geological time scales (Beall et al.,
65 2019; Gerya & Yuen, 2007; Meyer et al., 2017; Popov & Sobolev, 2008; Roy et al., 2021; Willis
66 et al., 2019).

67 The studies discussed in the preceding paragraph dealt with shear failure in mechanically
68 homogeneous solids. On the contrary, geological terrains can hardly be treated as homogeneous
69 continua as they mostly contain inherent compositional or mechanical heterogeneities on
70 macroscopic (e.g., igneous intrusives, faults or fracture zones, localized melt pockets, xenoliths)
71 to microscopic (e.g., intragranular fractures/cracks, soft mineral aggregates, strong xenocrysts)
72 scales. Field evidences, in fact, suggest that such heterogeneities can crucially influence the
73 process of shear localization (Grujic & Mancktelow, 1998; Pennacchioni & Mancktelow, 2007)
74 in forming isolated shear bands, as observed in analogue experiments (Grujic & Mancktelow,
75 1998; Mancktelow et al., 2002; Misra & Mandal, 2007). Laboratory experiments predicted the
76 geometry and orientations of shear bands that localize preferentially against mechanical flaws,
77 such as, voids and rigid inclusions (Misra & Mandal, 2007). Earlier studies, however, provided
78 little insights into the composite band evolution, characterized by multiple sets of primary and
79 secondary shear bands, as commonly observed in tectonic belts (Y. Katz et al., 2004; Meyer et

al., 2017; Misra & Mandal, 2007; Roy et al., 2021). The evolution of such complex internal band structures is virtually unexplored, and this gap motivates our present experimental study.

We conducted strain-rated controlled compression experiments on polystyrene (PS) sheets that under room temperature laboratory condition reproduced the typical plastic creep behaviour of common rocks reported from rock deformation experiments at elevated temperatures and pressures (B. K. Holtzman, Groebner, et al., 2003; B. K. Holtzman, Kohlstedt, et al., 2003; David L. Kohlstedt & Holtzman, 2009). From these experiments we demonstrate how pre-existing mechanically weak flaws can control the shear band mechanisms (numerous sharp narrow to composite wide band formation) in heterogeneous elasto-plastic rocks. We support our experimental findings with the results obtained from real scale numerical simulations within a framework of visco-elasto-plastic rheology. Finally, the article discusses a set of geological field examples of different types of internal band structures in the light of our laboratory experiments.

3. Laboratory studies

3.1. Experimental approach

Compressional test experiments (Fig 1a) were conducted on fabricated polystyrene (PS) models (Fig 1b) to study the mechanisms of shear band formation in laboratory conditions. We used commercial grade PS, which was selected after several trial experiments, ensuring that the material could produce sharp shear bands under our experimental conditions (room temperature and strain rates). Figure 1c shows its plastic creep behavior at slow ($2x10^{-5}$ s^{-1}) and relatively fast strain rates ($3x10^{-5}$ s^{-1}). The material yields at a stress of ~0.13 MPa at the low strain-rate, whereas at ~0.15MPa at the high strain-rate under the ambient temperature condition (27^{o}C). PS

samples containing circular mechanical flaws reduce their yield stresses to ~0.1MPa and ~0.12MPa at low and high strain rates, respectively (Fig 1c). We prepared the entire batch of PS models from the same PS sheet to avoid the possibility of any inherent variations in their rheological properties, e.g., yield strength, depending on the manufacturing history of the polymer.

A 9 mm thick, rectangular (60 mm x 35 mm) block was cut out from a large PS sheet, and its vertical face was drilled to create a through-going cylindrical hole of ~1mm diameter, as illustrated in Fig.1b. We then filled the hole with commercially available epoxy with an intention to replicate the secondary filling materials, as found in geological cavities and fractures. An epoxy of extremely low yield strength, compared to that of PS, was chosen to reproduce the mechanical setting of a weak flaw in the host. The models were left undisturbed overnight to allow the epoxy inside the hole to set in and form a mechanically weak solid region. The hole-normal vertical faces of the PS model were polished by P80 grit sandpaper to minimize the contact friction between the model block and the metal jig (Fig 1a). We gridded the vertical faces by passive 2 mm × 2 mm square grids to visualize the macro-scale heterogeneous strain fields around the hole in the deformed sample. Models were deformed under a hydraulically driven compression machine (Aimil Hydraulic Press, with 1200kN load frame), equipped to control the strain rate during an experimental run by a flow-controlled valve. We developed a specially designed sample housing system (jig) (Fig 1a) to run the deformation under a plane strain condition. The model was placed in the jig, keeping the flaw axis normal to the jig walls, and compressed with a vertical load (σ_1) under a biaxial stress condition, allowing the model to stretch perpendicular to the flaw axis (direction of no strain). To minimize the jig friction, we applied grease (viscosity 115 Pa s) at the model-jig wall interface prior to the beginning of model deformation. The experiments were run at ambient pressure and temperature (~27°C), keeping the σ_2 and σ_3 axes in horizontal directions, where σ_2 was oriented along the flaw axis direction

(Fig 1b). The vertical load (σ_1) was applied to the jig by moving the load frame in the upward direction against the stationary piston at the top, and continuously tracked by the 1200kN load cell attached at the top of the load frame. Under a given strain rate we ran a set of experiments for varying finite strains (6%, 12% and 18%) to study the progressive shear band structures with increasing deformation.

To study the role of pre-existing heterogeneity in shear band development, we first ran a set of reference experiments on homogeneous PS models (devoid of induced cylindrical flaw) and compared the results with those obtained from heterogeneous models. Both the homogeneous and the heterogeneous model experiments were conducted at low ($2x10^{-5}$ s^{-1}) and high ($3x10^{-5}$ s^{-1}) strain rates, with an aim to explore the possible effects of deformation rates on the mechanism of flaw-controlled shear band localization. Our compression experiments occasionally produced tensile fractures in the models during the sample unloading, which was minimized by keeping the PS model inside the jig and allowing the hydraulic pressure to release at an extremely slow rate ($2x10^{-3}$ mm/sec). After the successful unloading process, the model was cleaned and its vertical faces parallel to the σ_1-σ_3 plane were photographed to record the deformation patterns in the model, revealed from the deformed grids. We then post-processed the models for microscopic analyses, where each model was cut into thin slices (~0.5mm thick), perpendicular to the flaw axis, which was mounted on a glass slide. The thin section was observed under cross-polarized light to study the shear band patterns, characterized by their strong optical birefringence.

3.2. Experimental results

3.2. 1. Homogeneous models

Homogeneous PS models, deformed under high strain rates ($3x10^{-5}$ s^{-1}), produced numerous closely spaced, narrow shear bands (NBs), distributed more or less uniformly in the entire model region. Each band characteristically had exceptionally long (L), narrow (W) geometry ($L/W > 25$), defined by sharp boundaries (Fig 2a). They grew in length much faster than in width, as revealed from increasing L/W with model strain. The narrow bands form typically in conjugate sets (Fig 3a-i), with their dihedral angles (Φ) varying with increasing finite strain (ε). For $\varepsilon \sim 6\%$, the modal Φ lies in the range 70°-75°, which increases to ~80°-85° for $\varepsilon \sim$ 12%, and to ~85°-88° at $\varepsilon = 18\%$ (Fig 3b-i). Another interesting observation is that this type of bands multiplies in number to increase their P20 (Mauldon et al., 2001) estimated density (from $<4 \times 10^{-3}$ mm^{-2} at 6% to 18×10^{-3} mm^{-2} at 18%), with progressive compressional strains. To study such a spatio-temporal band evolution, we prepared band density maps from deformed models corresponding to $\varepsilon \sim 18\%$ (Fig. 3c-i), and found the following features: 1) the bands do not cluster in specific zones; they are more or less homogeneously distributed; 2) progressively increasing new band formation facilitates the degree of homogeneity; and 3) at large finite strains it is hard to recognize individual bands as the band density is extremely high. For large $\varepsilon > 18\%$, the PS model produced a few isolated domains that accommodated plastic strains in the bulk model, forming shear zones at a high angle to the compression direction (Fig 2a-iii).

Homogenous PS models deformed under lower strain rates ($2x10^{-5}$ s^{-1}) produced similar shear band geometry, implying that strain rate does not affect the mode of shear band growth in case of homogenous media. Detailed description is provided in Supplementary S1.

3.2.2. Heterogeneous models

Heterogeneous model experiments produced band structures markedly different from those formed in homogeneous models, irrespective of the strain rate ($\dot{\varepsilon}$) and the amount of finite strain (ε). However, $\dot{\varepsilon}$ critically controlled the mode of shear localization in the neighborhood of mechanical flaws, which we discuss later. Compression under high strain-rates ($\dot{\varepsilon}$ = 3 x 10^{-5} s^{-1}) developed plastic strains in the form of wide shear bands that localized preferentially at the extensional faces of the pre-existing heterogeneity. These plastic zones contained numerous narrow shear bands (NBs) in conjugate sets (Fig 3a-ii) with Φ = ~ 98° (Fig 3b-ii), forming a composite shear band (CB) structure (Fig 2b). In a CB one set of NBs formed nearly parallel or at low angles (~ 10° - 15°) to the overall CB trend, whereas the other at high angles (~ 85° - 95°), almost orthogonally oriented to the CB. Interestingly, the two sets had competing growth in the CB evolution; the low-angle set increased its band density by multiplying the number of NBs and at the same time grew in length to form a well-defined core zone, which was practically devoid of high-angle shear bands. Such a differential NB growth gave rise to a characteristic two-layer composite structure of CBs: a core zone of low-angle bands, flanked by zones of high-angle bands (called *transition zone* in the foregoing description). The transition zones represent an intermediate region between the strongly sheared core and the strain-free walls (revealed from weak or no optical birefringence and sharp termination of across-band NBs). Both the core and the transition zones increase their NB densities and formed a well-developed composite structure of CB at large ε (= 18%). A CB eventually shows a complete segregation of the two band populations in the core and the transition zones, which can be seen in the band density map (Fig 3c-ii). CBs had a lateral growth of their core zone at the cost of the transition zones, but they hardly change their overall band thickness. Consequently, the composite CB structure consistently increased the core/transition zone thickness ratio (T_r) with increasing ε, for example, T_r = 0.887 and 1.914 at ε = 6% and 18%, respectively.

To describe the overall band structure of a heterogeneous PS model under high strain rates ($\dot{\varepsilon}$ = 3 x 10^{-5} s^{-1}), each circular heterogeneity localizes a conjugate pair of CBs, symmetrically oriented at an angle of ~35° to the compression direction. Their core zones do not exactly follow the CB trend, but consistently form an oblique relation at an angle of ~10° to 15° (Fig. 2b-iii). They have dihedral angles (~75°), significantly lower than that of the corresponding CBs (~93°). As the loading progresses, the circular flaw is deformed into an oval shape and the CBs increase their dihedral angles by ~6°- 8°. The degree of shear partitioning between the core and transition zones of a CB, calculated from the across-band NB deflections, suggests contrasting shear localisation in the two domains of the CB. For a given model compression, e.g., ε = 6%, the estimated shear in the core is ~0.72, which becomes extremely low (~0.11) in the transition zone. However, the transition zones progressively increase their shear at a large finite deformation (ε = 18%), e.g. their estimated shear is ~0.31 when the finite shear at the core is ~1.2.

Under a low compression rate (2 x 10^{-5} s^{-1}) the same heterogeneous PS model produced a symmetrical pair of nearly tabular conjugate bands, radiating from the heterogeneity at an angle of ~40° to the compression direction (Fig 2c). In contrast to CBs, they are completely devoid of NBs, and develop distributed plastic strains, giving rise to the characteristics of homogeneous shear bands (HB). Secondly, the dihedral angle of HBs (Φ = ~80°) is lower than those of CBs. They have a narrow transition zone (T_r = ~0.3mm), revealed from the birefringence bands, on either side of the homogeneous core. The birefringence variations across the band length suggest a diffused boundary of the transition zone with the unstrained walls (Fig 2c-iii). Models at increasing ε from 6% to 18% show little modifications in the HBs, implying that they grow in thickness with increasing ε. Similarly, their transition zones remain unchanged, allowing the core zone to entirely accommodate the plastic strain in the model.

In summary, the PS model experiments lead us to recognize three distinct types of shear band structures: narrow bands (NBs), wide composite bands (CBs) and wide homogeneous bands (HBs) (Fig 4). NBs are defined by their extremely long, narrow band geometry ($L/W > 25$) with sharp boundaries (Fig 4a). They occur as densely penetrative band structures in a homogeneous medium. The presence of a mechanical heterogeneity results in a transition of the shear localization mechanism to form either CBs or HBs, depending on the bulk strain rates ($\dot{\varepsilon}$). A CB consists of two orthogonal sets of NBs, forming a composite structure: core (cluster of densely packed, sub-parallel NBs that accommodates maximum plastic strain) and transition zones (set of closely spaced orthogonal NBs showing shear drags) (Fig 4b). A HB, produced relatively at lower strain rate, is characterized by a thick band of homogenous shear localization, bounded by narrow zones showing gradational shear boundary with the walls (Fig 4c).

4. Numerical modelling

4.1. Theoretical considerations

We develop 2D finite element (FE) models to reproduce the mechanisms of shear band localization as a function of mechanical heterogeneities on the natural scale, with an aim to show the validity of our laboratory interpretations for geological strain rates. The FE modelling uses the open-source, particle-in-cell, finite element code Underworld2 (http://www.underworldcode.org/) that solves the incompressible Stokes equations for visco-plastic materials in combination with the energy conservation equation (Mansour et al., 2020; Moresi et al., 2007). We consider a rectangular, visco-elasto-plastic domain in a Cartesian space subjected to pure shear deformation (Fig 5a), as in the laboratory setting. We choose a 1D rheological model, consisting of an elastic (spring), a plastic (frictional block) and a viscous (dashpot) element in series (Fig 5b). The Drucker-Prager yield criterion is chosen to set plastic

strain localization in the FE model at a threshold stress. The model domain is discretized into quadrilateral meshes, comprising 564 x 328 elements. We performed mesh refinement tests to find the level of mesh resolution required to attain a steady model output, implying that the simulation results hardly changed with further mesh refinement.

To model the plastic yielding condition, we consider the first and second invariants of stress tensor (σ_{ij}):

$$I_1 = \sigma_{jj}; \quad (1)$$

$$I_2 = \frac{\sigma_{ii}\sigma_{jj} - \sigma_{ij}\sigma_{ij}}{2} \quad (2)$$

Decomposing σ_{ij} into the isotropic (${\sigma^o}_{ij}$) and the deviatoric stress (${\sigma^s}_{ij}$) tensors, it follows

$${\sigma^o}_{ij} = \frac{1}{3}\sigma_{kk}\delta_{ij} \text{ and } {\sigma^s}_{ij} = \sigma_{ij} - {\sigma^o}_{ij}, \quad (3)$$

where δ_{ij} is Kronecker delta. From Eq. (2) and (3), the second stress invariant, I_2 is expressed as

$$I_2 = 3{{\sigma^o}_{jj}}^2 - \frac{1}{2}\sigma_{ij}\sigma_{ij} \quad (4)$$

Considering incompressible rheology, the total strain-rate tensor is a sum of elastic ($\dot{\varepsilon}^e_{ij}$), plastic ($\dot{\varepsilon}^p_{ij}$) and viscous ($\dot{\varepsilon}^v_{ij}$) strain-rates:

$$\dot{\varepsilon}_{ij} = \dot{\varepsilon}^v_{ij} + \dot{\varepsilon}^p_{ij} + \dot{\varepsilon}^e_{ij}, \quad (5)$$

where $\dot{\varepsilon}^v_{ij} = \frac{1}{2}\frac{{\sigma^s}_{ij}}{\eta_v}$,

$$\dot{\varepsilon}^p_{ij} = \begin{cases} 0, & I_2 < \sigma_{yield} \\ \chi\left(\frac{1}{2}\frac{{\sigma^s}_{ij}}{I_2}\right), & I_2 \geq \sigma_{yeild} \end{cases},$$

$$\dot{\varepsilon}^e_{ij} = \frac{1}{2G}\frac{D{\sigma^s}_{ij}}{Dt}$$

σ_{yeild} denotes the yield strength of the material, G is the Elastic shear module, η_v is the bulk viscosity of the material, and χ is a plastic multiplier, satisfying the yield condition, $I_2 = \sigma_{yeild}$.

In the FE modelling we introduce post-yield viscous weakening of the material (strain softening rheology), where the modified viscosity decreases nonlinearly with increasing strain. This synkinematic rheological transformation is implemented by expressing the effective current viscosity as a function of strain rate and the yield stress,

$$\eta_{eff} = \frac{\sigma^s{}_{ij}}{2|\dot{\varepsilon}|}, \quad (6)$$

where $|\dot{\varepsilon}|$ is the second invariant of the strain rate tensor.

As the model domain is chosen to replicate a portion of the crust, we consider a linear dependence of the yield limit (σ_{yield}) on lithostatic pressure (p), similar to the Drucker-Prager plasticity criterion. This is comparable to the Mohr-Coulomb plasticity in 2-D for incompressible plane strain deformation (Roy et al., 2021; Snell et al., 2020), written as

$$\sigma_{yield} = C(\gamma_{pl}) + tan\emptyset p\,, \quad (7)$$

where $p = -\frac{1}{3}I_1$, and $C(\gamma_{pl})$ is the material cohesion, expressed as a function of plastic strain γ_{pl} , and $\emptyset$ is the angle of internal friction. The cohesion is assumed to weaken with increasing accumulated plastic strain:

$$C = C_i + (C_f - C_i)\min(1, \frac{\gamma_{pl}}{\gamma_o}), \quad (8)$$

where C_i is the initial cohesion and C_f is the final cohesion of the shear zone material. Also, $\gamma_{pl} = \int_0^t \dot{\varepsilon}_p\, dt$, indicates accumulated plastic strain in regions where the yield limit is reached

and $\gamma_o = 0.1$ is taken as the reference strain. No syn-deformational healing of the cohesion is implemented in this model.

4.2. Shear band simulations

We performed three different sets of numerical simulations: 1) Model Simulations (MS1) to reproduce the reference laboratory experiments with homogeneous PS models; 2) Model Simulation (MS2) to replicate heterogeneous laboratory model containing a circular cylindrical flaw at high strain rates ($\dot{\varepsilon}$ = 2 x 10^{-12} s^{-1}), and 3) Model Simulation (MS3) similar to MS2, but run at a significantly low strain rates ($\dot{\varepsilon}$ = 5 x 10^{-14} s^{-1}). Figure 5c presents the typical stress-strain curves obtained from these three kinds of model simulations run at room temperature, where all of them show the stress to rise with increasing finite strain and reach the maximum yield stress, followed by a drop to the lower yield stress. This stress variation broadly agrees with the laboratory findings. The simulated models start to produce narrow shear bands (NBs) at finite strains of about 3% - 4%, which commences prior to a proportionality limit of the stress-strain curve. However, NBs appear in large density only when the upper yield stress is attained at about 6% -7% strain. Sporadic NBs that initiated at a pre-upper yield stress might have resulted from local stress concentrations due to some mesh configurations.

MS 1: The homogeneous model initially (ε = ~4%) produced two sets of narrow shear bands (NBs), symmetrically oriented to the compression direction with a dihedral angle (Φ) of ~70°. They do not cluster in specific locations, but show a uniform spatial distribution in the model domain. They grow in length and at the same time, multiply in number to increase their spatial density with increasing ε (Fig 6a). We calculated strain profiles along a number of transects in the simulated band structures to find the spatial patterns of band distributions (Fig 6a-i). A profile for ε = 5% does not show any peaks (Fig 7a-i), i.e., strain perturbations by shear band formation. In an advanced stage (ε > 10%) the simulation produces numerous peaks that

amplify with increasing ε, but remain in low amplitudes (Fig 7a). Their spatial patterns suggest a distributed development of band structures in the model simulations at ε = 15 – 20% (Fig. 7a-iv). However, a few bands selectively localise larger plastic strains, and gain prominence in the matrix of homogeneously distributed numerous bands. The shear bands hardly widen with progressive deformations.

MS 2: This simulation run at a higher strain-rate generates a pair of composite shear bands, radiating from the flaw boundary at a model strain (ε) < 5% (Fig 6b). The shear bands are symmetrically oriented at an angle of ~40° to the compression direction, forming $\Phi \sim 80°$. A close view of the model reveals a characteristic internal structure of the conjugate bands, each of them forms a narrow core zone of the greatest plastic strains, oriented obliquely to the overall band trend, as observed in CBs of the laboratory experiments (Fig 6b-iii). Two core zones on either flank of the flaw thus form a dihedral angle ($\Phi \sim 75°$) lower than that described by the overall conjugate band structures. They continue to accumulate plastic strain, leaving the rest part relatively unstrained. This model shows partitioning of the plastic strain equally into two parallel pairs of identical bands. Strain profile across the model (Supplementary S2) shows four distinct and almost equal peaks which demonstrates that the plastic deformation is accommodated into several bands (~4) of equal intensity.

MS 3: The simulation at a low model strain rate produces a pair of conjugate shear bands ($\Phi \sim 75°$) that localize preferentially at the extensional flaw boundary when (ε < 5%) (Fig 6c-i), as manifested in two high-amplitude, sharp peaks in the corresponding strain profile (Fig 7b, c). The time series simulations reveal that each shear band grows in length and concurrently multiplies the magnitudes of their maximum strain localization, eventually to form a core of homogeneously distributed strain, as observed in experimental HBs. Such a band evolution is well reflected from the corresponding strain profiles (Fig 7), marked by two outstanding peaks of

329 nearly equal amplitudes in the low-amplitude spectrum. The peak density distribution indicates a
330 large part of plastic strain partitioning selectively in the flaw-controlled conjugate bands. As the
331 model deformation progresses, the circular flaw is deformed into an elliptical shape, and the
332 model produces several secondary shear bands, although of much lower thickness in conjugate
333 sets at $\varepsilon > 15\%$ (Fig 6c-iii). This complex band structure is evident from multiple peaks in the
334 strain profiles (Fig. 7c-iv), where the secondary peaks have amplitudes much lower than the
335 principal peaks, implying that the flaw-controlled bands mainly accommodate the bulk strain,
336 even after localization of the secondary bands. The calculated stress-strain curve (Fig 5c) for
337 MS3 indicates that the heterogeneous model attains the state of complete failure much earlier
338 than MS1.

339

340 **5. Geological relevance**

341 *5.1. Field study approach*

342 Both the laboratory experiments and FE model simulations suggest that pre-existing
343 mechanical flaws are necessary agents to form isolated shear band/zones, as commonly
344 encountered in most of the geological terrains. A flaw-free, homogeneous rock at the yield stress
345 would produce numerous, spatially distributed narrow shear bands (cf. NBs observed in
346 homogeneous PS experiments), but not isolated wide shear zones in host rocks. However, it is
347 difficult to recognize the nucleation of a shear zone in relation to pre-existing flaws in the field
348 because the length scale of shear zones eventually far exceeds the flaw dimension, leaving the
349 flaws geometrically almost unrecognizable objects, as seen in the numerical simulations (Fig 6).
350 But, some of their characteristic features can reflect their flaw-controlled origin. We discuss here
351 outcrop scale shear zones from the Chotonagpur Granite Gneissic Complex (CGGC) in the light
352 of our heterogeneous model experiments. We chose three locations in the CGGC: 1) Bero

353 Hillocks (23°32'09.5" N, 86°40'01.3" E) near Raghunathpur town, 2) outcrops on the Purulia-
354 Asansol Road transect near Baraseni (23°25'20.9"N 86°28'48.8"E), and 3) Jasidih (24° 31′ 19.2″
355 N, 86° 38′ 51.72″ E) (Supplementary S3). The CGGC terrain consists of a variety of country
356 rocks, such as porphyritic granite gneisses, khondalite, amphibolite and mafic granulite. Our
357 field studies concentrated in shear zones within banded and augen granite gneisses. An elaborate
358 description of the CGGC is provided in Supplementary S3.

359

360 *5.2. Field observations and their analysis*

361 Three distinct types of shear zones were recognized based on their internal shear
362 structures and the nature of contact with the relatively less deformed host rock: Type I – isolated,
363 narrow shear zones with maximum shear focused in the central zone, forming sharp boundaries
364 with the unsheared walls (Fig 8a), Type II – broad shear zones, consisting of a sheared core,
365 defined by a cluster of narrow shear bands, where the entire composite structure is bounded by a
366 drag zone on its either side (Fig 8b), and Type III - thick homogeneous shear zones with a
367 narrow diffused zone, forming a gradational boundary with the unsheared host (Fig 8 c). As
368 these contrasting types occur in the same rocks, the lithology does not seem to be a prime factor
369 in controlling the varying modes of band formation in our study area.

370 Type I shear structures, observed in an outcrop of garnet-bearing quartzo-feldspathic
371 gneissic rocks (location 2) near Purulia town, characteristically show intense shear localization (ε
372 > 12) in narrow (thickness: ~2mm - ~5cm), linear zones, with their strike length on a few
373 centimeters (Fig. 8a). High-resolution structural mapping {scale 1:100} (Fig 9a-i) reveals that
374 they are spatially distributed over the entire outcrop, and their statistical orientations define a
375 conjugate set (Fig 9a-ii) with a dihedral angle of ~70°-75° (Fig 9a-iii). In overall, this type of
376 shear zones resembles narrow shear bands (NBs) produced in homogeneous PS models (Fig 2a)

and numerical simulations (Fig 6a) that typically show an abrupt transition of shear strain across them (Fig 9b-i), without showing any significant drag zone. In many places of our study area, such as Raghunathpur - Bero Hills (Location 1) and Jasidih (Location 3) we observed Type II shear zones in granite gneissic hosts. This type of shear zone structures often localizes against quartzo-feldshapthic lenses in conjugate sets (Fig 8b), as in the heterogeneous PS model experiments under high compression rates (Fig. 2b). The bands contain a strongly sheared core (~20 – 50 cm), flanked by wide transition zones (~5-10 cm to ~1-2 m) that gradually reduce shear strain from the core to unsheared walls. Although the shear zones are devoid of orthogonal NBs on macro-scales, they form typically a core - drag zone complex structure, which is comparable to CBs produced in the heterogeneous PS models at high shear rates (Fig 2b). Type III shear zones contain a thick, homogeneously sheared core (~15-20cm), bordered by a narrow zone of gradational shear on either side of the core (Fig 8c). They look like flaw-controlled HBs in PS experiments under relatively slow rates. Both Type II and III shear zones had long strike lengths, ranging from a fraction to tens of meters, irrespective of their core thickness. Type II strain profiles reveal gradational shear strain variation from the unsheared wall to core, forming a bell like pattern (Fig 9 b-ii, Details in Supplementary S4). In contrast, Type III is characterized by a plateau-like structure of their strain profiles (Fig 9b-iii).

6. Discussions

6.1. Physical factors controlling the band growth patterns

Earlier studies demonstrated the evolution of micro-bands (cf. NBs) from plane-strain compression experiments on various solids, such as steels and polymers (Anand & Spitzig, 1982; Bowden & Raha, 1970). The micro-bands generally multiply their number with increasing compressional strain, hardly showing any growth in thickness. Bowden and Raha's (1970)

401 elaborate experiments with PMMA and PS show a transition from micro- to diffuse shear band
402 formation as a function of temperature and strain rate. For example, their experiments find the
403 micro-band mechanism as the dominant mechanism of plastic strain localization in PS at room
404 temperature (21°C), completely replaced by diffuse shear bands at higher temperatures (60°C to
405 70°C). They showed the same transition by lowering the strain-rate of the test from 2.3 x 10^{-2}
406 sec^{-1} to 6.0 x10^{-3} sec^{-1}. These experimental results can be used to predict the band transition
407 conditions, in terms of thermal or kinematic conditions, but it is applicable for mechanically
408 homogeneous materials. Rocks and natural materials, such as soils are, however, heterogeneous
409 due to various geological reasons (discussed later), and their heterogeneities can largely
410 influence the process of shear-band formation in them (Grujic & Mancktelow, 1998;
411 Pennacchioni & Mancktelow, 2007). We thus include pre-existing heterogeneities as an
412 additional factor in this study, with an aim to widen the applicability of the previous
413 experimental findings for inherently heterogeneous material systems. Our PS model experiments
414 suggest that the presence of mechanical flaws can result in a transition of the shear band
415 mechanism under the same temperature and bulk strain conditions. For example, homogeneous
416 PS models produce spatially distributed narrow shear bands (cf. micro-bands of Bowden and
417 Raha) with a dihedral angle ~85° at room temperature condition and a strain rate of 3 x 10^{-5} sec^{-1}
418 (Fig 2a). The same experimental condition produces band formation in a localized mode,
419 forming a composite band (CB) structure when the material contains a tiny circular flaw. The
420 CBs form in conjugate sets with a dihedral angle of ~86°-90°. It follows from this discussion that
421 the transition from distributed to localized band formation may not always reflect a drop in strain
422 rate or lowering in temperature, as interpreted in earlier studies (Bowden & Raha, 1970). This
423 can occur in the same location under the same physical condition, depending on the availability
424 of inherent mechanical heterogeneities, as observed in our study area discussed in the preceding
425 section. Structural overprinting relations, e.g. shear localization and foliation of particular

426 generations, suggest that they formed in the same phase of deformation. In addition, the
427 temperature and the strain rate conditions are unlikely to change to a large extent in an outcrop or
428 a small part of the study area. We suggest that varying shear band patterns observed in the
429 CGGC might have originated from inherent mechanical heterogeneities in gneissic granites.

430

431

432 *6.2. Geological origin of mechanical heterogeneities*

433 Geological terrains evolve through complex petrogenetic and tectonic processes that
434 eventually result in heterogeneous characteristics of the rocks on a wide range of scales: micro-
435 scale, such as mechanically contrasting mineral grains and grain scale fractures, to kilometer
436 scales, such as magma bodies (plutons) and fault zones. This study deals with weak flaws in a
437 continuum, as they represent the most common type of mechanical heterogeneities encountered
438 in the rock systems. This discussion thus focuses upon the origin of mechanically weak flaws in
439 crustal rocks. A group of such flaws originate from petrological processes, such as partial
440 melting, hydrothermal fluid enrichment and localized hydrolytic weakening. Partial melting in
441 high-grade metamorphic conditions (p = ~3-4 Kb and T = ~750°C – 900°C) produces isolated
442 melt pockets on macroscopic scale (a few millimeters to several centimeters), as reported from
443 many field studies (Dijkstra et al., 2002; Kelemen & Dick, 1995; Lee et al., 2018; Piazolo et al.,
444 2020). Both theoretical and experimental estimates suggest that the viscosity of quartzo-
445 feldspathic melts ranges 3.9 x 10^{-3} to 1 x 10^{-2} Pa s, depending upon the volume content of solid
446 crystals in them (Holtz et al., 1999). Assuming the viscosity of granitic crust in the order of 10^{21}
447 Pa s at the corresponding P-T condition (D. L. Kohlstedt, 2007), the viscosity ratio of melt
448 pockets to their host is found to be extremely low (~0.22), implying that the melt pockets would
449 mechanically act almost like holes in the bulk rocks, similar to the consideration in the PS

models. Interestingly, such weak zones can be effective agents to localize outcrop scale shear zones in metamorphic terrains. Hydrothermal alteration is another important weak-zone forming mechanism at shallow to mid-crustal depths (Adak et al., 2021; Kalczynski & Gates, 2014; Rolland et al., 2003). Such alteration generally produces a variety of phyllosilicates, depending upon the geochemical composition and temperature of the hydrothermal fluids. Experimental studies suggest that phyllosilicate enrichments can lower the viscosity by several orders (Misra, Burlini, et al., 2009), forming isolated weak mechanical heterogeneities, especially in crustal terrains that undergo intense fluid activities, as imprinted in abundant pegmatitic bodies.

Another group of weak heterogeneities originate from mechanical processes, such as crack development and fracturing of rocks. Tensile fractures, for example, often form with a finite length, and they subsequently open out, forming lenticular zones, filled with leucosome materials. Field studies have reported localization of conjugate shear zones against such leucosome pods (Grujic & Mancktelow, 1998) and nodal veins of boudinage structures, formed by tensile fractures. With continued deformations the opening fractures act as weak zones to cause stress concentrations (Misra, Mandal, et al., 2009). Such mechanical heterogeneities provide seeds for preferential plastic yielding to initiate shear bands in the bulk continua (Eshelby, 1959; Rutter et al., 1986), as also reported in several geological studies (Grujic & Mancktelow, 1998; Meyer et al., 2017; Misra & Mandal, 2007; Roy et al., 2021). This article advances this line of study by showing the role of weak zones to shear band formation in three mechanisms: distributed narrow shear bands (NBs), localized composite shear bands (CBs) and internally homogeneous shear bands (HBs) as the typical patterns of the shear zones formed due to mechanical heterogeneities.

6.3. Macroscopic rheology in shear zone modelling

To model purely ductile or brittle-ductile shear zones in rocks, the crucial step demands an appropriate rheological framework with a close approximation to the geological conditions of interest (Bercovici & Karato, 2002; Gerya & Yuen, 2007; Popov & Sobolev, 2008). Previous works have used a wide spectrum of rheologies in shear zone modelling, ranging from power-law viscous (Fleitout & Froidevaux, 1980; D. A. Yuen et al., 1978; David A. Yuen & Schubert, 1977) to complex visco-elasto-plastic rheology (Babeyko & Sobolev, 2008; Gerya & Yuen, 2007; Kaus, 2010). However, visco-plastic and elasto-plastic rheologies are perhaps the most commonly used rheological classes. Both of them have certain drawbacks for ductile shear zone modeling. On one hand, the non-associative plasticity for visco-plastic media applies to weak and narrow brittle fault zones that can hardly represent the entire lithosphere. Furthermore, modelling based on this rheological consideration produces transient shear bands that fail to grow steadily to attain a mature state as they are immediately replaced by new generation of bands in the course of progressive deformation (Regenauer-Lieb & Yuen, 2003). The other drawback concerns the exaggeration of brittle responses in the model over the ductile contribution that critically determines the growth of shear zones in ductile or brittle-ductile regimes, as applicable to lithospheric deformations. To overcome these shortcomings, we use an elasto-visco-plastic rheology to model ductile shear zones around a weak zone. This rheological approximation simulates them in agreement with the field observations reported earlier (Grujic & Mancktelow, 1998; Meyer et al., 2017; Misra & Mandal, 2007; Roy et al., 2021) and in this study.

6.4. Limitations

This study is entirely based on laboratory experiments run at room temperature, and excludes the possible effects of temperature on shear band growth, as the main aim targets at understanding how a mechanical heterogeneity can independently mediate the mechanism of

shear band localization in a rock under compression. Previous studies e.g., (Bowden & Raha, 1970) have demonstrated from experiments that the temperature can largely influence the shear band pattern. Further experimental investigations, combining the effects of temperature and mechanical flaws, can provide a better approximation to actual geological conditions. Secondly, both the laboratory experiments and numerical modelling accounts for pure shear to represent the bulk deformations. Field studies reported shear zone development in complex tectonic settings, such as transpression where simple shear acts a major component in the bulk rock deformations. Many rocks develop tectonic fabrics, such as foliation either prior or during the event of shear zone formation. Such fabrics can introduce mechanical anisotropy in the bulk rocks. Our study does not explore the possible role of such anisotropy in the shear band growth around weak zones, which is a limitation and opens a scope for further investigation.

7. Conclusions

1) Analogue laboratory experiments confirm earlier geological observations that inherent mechanical heterogeneities in rocks act as potential nucleating seeds for shear zone formation. At a threshold stress rocks and similar solids without any inherent heterogeneities would always produce spatially distributed numerous narrow, sharp bands (NBs) in conjugate sets with a dihedral angle of ~75°-85° to the compression direction. Their overall pattern is unlike isolated or solitary wide shear zones commonly observed in tectonic belts.

2) In homogeneous solids NBs begin to form at ~5% finite strain and multiply in number to increase their spatial density with increasing finite strain, and at the same time they grow in length with nearly a constant thickness.

3) The presence of weak heterogeneities results in a transition of spatially distributed NBs to isolated wide composite shear bands (CBs). The CBs radiate from the circular flaw in conjugate pairs with a dihedral angle of ~85°-90°. A typical CB develops a characteristic internal band

structures, consisting of a strongly sheared core (cluster of extremely close spaced sub-parallel NBs, flanked by a region of orthogonal NBs on either side of it. The CB core accommodates most of the plastic strain in the band, leaving its flank regions for weak shear localization.

4) The mechanism of heterogeneity-controlled shear band localization is sensitive to the global strain rate ($\dot{\varepsilon}$). Reducing $\dot{\varepsilon}$ replaces composites bands (CBs) with wide, homogeneous shear bands (HBs), which are completely devoid of NBs.

5) The real scale (both space and time) 2D finite element models, based on visco-elasto plastic rheology validate the following laboratory findings: 1) transition in the mechanism of band formation (spatially distributed NBs to localized CBs) depending on the absence or presence of an inherent weak flaw, and 2) CB to HB transformation with reducing global strain rates.

5) Heterogeneous mechanical models explain the diverse types of shear zones commonly observed in many geological terrains, like CGGC.

Acknowledgements

The present work has been supported by the SERB-DST, Government of India, with J. C. Bose Fellowship (SR/S2/JCB-36/ 2012) to N. M. and by the BRNS with a research project (36(2)/14/25/2016- BRNS). CSIR, India is gratefully acknowledged for awarding research fellowship grants to A. Roy (09/096(0940)/2018-EMR-I).

Data Availability Statement

The relevant data supporting the conclusions are present in this manuscript and in the supplementary information. All aspects of UNDERWORLD 2 can be downloaded and checked here (https://www.underworldcode.org/).

References

Adak, S., Pal, D. C., Upadhyay, D., & Mondal, R. (2021). Textural re-equilibration, hydrothermal alteration and element redistribution in Fe-Ti oxide pods, Singhbhum Shear Zone, eastern India. *Geochemistry*, *81*(1), 125679. https://doi.org/10.1016/j.chemer.2020.125679

Anand, L., & Spitzig, W. A. (1980). Initiation of localized shear bands in plane strain. *Journal of the Mechanics and Physics of Solids*, *28*(2), 113–128. https://doi.org/10.1016/0022-5096(80)90017-4

Anand, L., & Spitzig, W. A. (1982). Shear-Band Orientations in Plane Strain. *Acta Metallurgica*, *30*(2), 553–561.

Babeyko, A. Y., & Sobolev, S. V. (2008). High-resolution numerical modeling of stress distribution in visco-elasto-plastic subducting slabs. *Lithos*, *103*(1–2), 205–216. https://doi.org/10.1016/j.lithos.2007.09.015

Bauer, H., Rogowitz, A., Grasemann, B., & Decker, K. (2018). Intracrystalline deformation of calcite in the upper brittle crust. *Geology*, *46*(4), 375–378. https://doi.org/10.1130/G39990.1

Beall, A., Fagereng, Å., & Ellis, S. (2019). Fracture and Weakening of Jammed Subduction Shear Zones, Leading to the Generation of Slow Slip Events. *Geochemistry, Geophysics, Geosystems*, *20*(11), 4869–4884. https://doi.org/10.1029/2019GC008481

Bercovici, D., & Karato, S. I. (2002). Theoretical analysis of shear localization in the lithosphere. *Reviews in Mineralogy and Geochemistry*. https://doi.org/10.2138/gsrmg.51.1.387

Bowden, P. B., & Raha, S. (1970). The formation of micro shear bands in polystyrene and polymethylmethacrylate. *Philosophical Magazine*, *22*(177), 463–482. https://doi.org/10.1080/14786437008225837

Camwell, L., & Hull, D. (1973). Crazing and fracture associated with the interaction of shear bands in polystyrene. *Philosophical Magazine*, *27*(5), 1135–1150. https://doi.org/10.1080/14786437308225822

Condit, C. B., & Mahan, K. H. (2018). Fracturing, fluid flow and shear zone development: Relationships between chemical and mechanical processes in Proterozoic mafic dykes from southwestern Montana, <scp>USA</scp>. *Journal of Metamorphic Geology*, *36*(2), 195–223. https://doi.org/10.1111/jmg.12289

Dijkstra, A. H., Drury, M. R., & Frijhoff, R. M. (2002). Microstructures and lattice fabrics in the Hilti mantle section (Oman Ophiolite): Evidence for shear localization and melt weakening in the crust-mantle transition zone? *Journal of Geophysical Research: Solid Earth*, *107*(B11), ETG 2-1-ETG 2-18. https://doi.org/10.1029/2001jb000458

Eshelby, J. D. (1959). The elastic field outside an ellipsoidal inclusion. *Proceedings of the Royal Society of London. Series A. Mathematical and Physical Sciences*, *252*(1271), 561–569. https://doi.org/10.1098/rspa.1959.0173

Fleitout, L., & Froidevaux, C. (1980). Thermal and mechanical evolution of shear zones. *Journal of Structural Geology*, *2*(1–2), 159–164. https://doi.org/10.1016/0191-8141(80)90046-2

583 Fossen, H. (2010). *Structural Geology*. Cambridge University Press.

584 Fossen, Haakon, & Cavalcante, G. C. G. (2017). Shear zones – A review. *Earth-Science*
585 *Reviews*, *171*(May), 434–455. https://doi.org/10.1016/j.earscirev.2017.05.002

586 Gerya, T. V., & Yuen, D. A. (2007). Robust characteristics method for modelling multiphase
587 visco-elasto-plastic thermo-mechanical problems. *Physics of the Earth and Planetary*
588 *Interiors*, *163*(1–4), 83–105. https://doi.org/10.1016/j.pepi.2007.04.015

589 Grujic, D., & Mancktelow, N. S. (1998). Melt-bearing shear zones: analogue experiments and
590 comparison with examples from southern Madagascar. *Journal of Structural Geology*,
591 *20*(6), 673–680. https://doi.org/10.1016/S0191-8141(98)00006-6

592 Holtz, F., Roux, J., Ohlhorst, S., Behrens, H., & Schulze, F. (1999). The effects of silica and
593 water on the viscosity of hydrous quartzofeldspathic melts. *American Mineralogist*, *84*(1–
594 2), 27–36. https://doi.org/10.2138/am-1999-1-203

595 Holtzman, B. K., Kohlstedt, D. L., Zimmerman, M. E., Heidelbach, F., Hiraga, T., & Hustoft, J.
596 (2003). Melt segregation and strain partitioning: Implications for seismic anisotropy and
597 mantle flow. *Science*, *301*(5637), 1227–1230. https://doi.org/10.1126/science.1087132

598 Holtzman, B. K., Groebner, N. J., Zimmerman, M. E., Ginsberg, S. B., & Kohlstedt, D. L.
599 (2003). Stress-driven melt segregation in partially molten rocks. *Geochemistry, Geophysics,*
600 *Geosystems*, *4*(5). https://doi.org/10.1029/2001GC000258

601 Holtzman, Benjamin K., Kohlsted, D. L., & Morgan, J. P. (2005). Viscous energy dissipation
602 and strain partitioning in partially molten rocks. *Journal of Petrology*, *46*(12), 2569–2592.
603 https://doi.org/10.1093/petrology/egi065

604 Hutchinson, J. W., & Tvergaard, V. (1980). Surface instabilities on statically strained plastic
605 solids. *International Journal of Mechanical Sciences*, *22*(6), 339–354.

606 Kalczynski, M. J., & Gates, A. E. (2014). Hydrothermal alteration, mass transfer and magnetite
607 mineralization in dextral shear zones, western Hudson Highlands, New York, United States.
608 *Ore Geology Reviews*, *61*, 226–247. https://doi.org/10.1016/j.oregeorev.2014.02.007

609 Katz, R. F., Spiegelman, M., & Holtzman, B. (2006). The dynamics of melt and shear
610 localization in partially molten aggregates. *Nature*, *442*(7103), 676–679.
611 https://doi.org/10.1038/nature05039

612 Katz, Y., Weinberger, R., & Aydin, A. (2004). Geometry and kinematic evolution of Riedel
613 shear structures, Capitol Reef National Park, Utah. *Journal of Structural Geology*, *26*(3),
614 491–501. https://doi.org/10.1016/j.jsg.2003.08.003

615 Kaus, B. J. P. (2010). Factors that control the angle of shear bands in geodynamic numerical
616 models of brittle deformation. *Tectonophysics*, *484*(1–4), 36–47.
617 https://doi.org/10.1016/j.tecto.2009.08.042

618 Kelemen, P. B., & Dick, H. J. B. (1995). Focused melt flow and localized deformation in the
619 upper mantle: juxtaposition of replacive dunite and ductile shear zones in the Josephine
620 peridotite, SW Oregon. *Journal of Geophysical Research*, *100*(B1), 423–438.
621 https://doi.org/10.1029/94JB02063

622 Kohlstedt, D. L. (2007). Properties of Rocks and Minerals - Constitutive Equations, Rheological
623 Behavior, and Viscosity of Rocks. *Treatise on Geophysics*, *2*, 389–417.

https://doi.org/10.1016/B978-044452748-6.00043-2

Kohlstedt, David L., & Holtzman, B. K. (2009). Shearing melt out of the earth: An experimentalist's perspective on the influence of deformation on melt extraction. *Annual Review of Earth and Planetary Sciences*, *37*, 561–593. https://doi.org/10.1146/annurev.earth.031208.100104

Lee, A. L., Torvela, T., Lloyd, G. E., & Walker, A. M. (2018). Melt organisation and strain partitioning in the lower crust. *Journal of Structural Geology*. https://doi.org/10.1016/j.jsg.2018.05.016

Mancktelow, N. S., & Pennacchioni, G. (2005). The control of precursor brittle fracture and fluid-rock interaction on the development of single and paired ductile shear zones. *Journal of Structural Geology*, *27*(4), 645–661. https://doi.org/10.1016/j.jsg.2004.12.001

Mancktelow, N. S., Arbaret, L., & Pennacchioni, G. (2002). Experimental observations on the effect of interface slip on rotation and stabilisation of rigid particles in simple shear and a comparisons with natural mylonites. *Journal of Structural Geology*, *24*(3), 567–585. https://doi.org/10.1016/S0191-8141(01)00084-0

Mansour, J., Giordani, J., Moresi, L., Beucher, R., Kaluza, O., Velic, M., et al. (2020). Underworld2: Python geodynamics modelling for desktop, HPC and cloud. *Journal of Open Source Software*, *5*(47). https://doi.org/10.1130/G39943.1

Mauldon, M., Dunne, W. M., & Rohrbaugh, M. B. (2001). Circular scanlines and circular windows: New tools for characterizing the geometry of fracture traces. *Journal of Structural Geology*, *23*(2–3), 247–258. https://doi.org/10.1016/S0191-8141(00)00094-8

Meyer, S. E., Kaus, B. J. P., & Passchier, C. (2017). Development of branching brittle and ductile shear zones: A numerical study. *Geochemistry, Geophysics, Geosystems*, *18*, 2054–2075. https://doi.org/10.1002/2016GC006793.Received

Misra, S., & Mandal, N. (2007). Localization of plastic zones in rocks around rigid inclusions: Insights from experimental and theoretical models. *Journal of Geophysical Research: Solid Earth*, *112*(9), 1–15. https://doi.org/10.1029/2006JB004328

Misra, S., Mandal, N., & Chakraborty, C. (2009). Formation of Riedel shear fractures in granular materials: Findings from analogue shear experiments and theoretical analyses. *Tectonophysics*, *471*(3–4), 253–259. https://doi.org/10.1016/j.tecto.2009.02.017

Misra, S., Burlini, L., & Burg, J. P. (2009). Strain localization and melt segregation in deforming metapelites. *Physics of the Earth and Planetary Interiors*, *177*(3–4), 173–179. https://doi.org/10.1016/j.pepi.2009.08.011

Mitchell, T. M., & Faulkner, D. R. (2009). The nature and origin of off-fault damage surrounding strike-slip fault zones with a wide range of displacements: A field study from the Atacama fault system, northern Chile. *Journal of Structural Geology*, *31*(8), 802–816. https://doi.org/10.1016/j.jsg.2009.05.002

Moresi, L., Quenette, S., Lemiale, V., Mériaux, C., Appelbe, B., & Mühlhaus, H. B. (2007). Computational approaches to studying non-linear dynamics of the crust and mantle. *Physics of the Earth and Planetary Interiors*, *163*(1–4), 69–82. https://doi.org/10.1016/j.pepi.2007.06.009

Nizolek, T. J., Pollock, T. M., & McMeeking, R. M. (2021). Kink band and shear band

localization in anisotropic perfectly plastic solids. *Journal of the Mechanics and Physics of Solids*, *146*(July 2019), 104183. https://doi.org/10.1016/j.jmps.2020.104183

Pennacchioni, G., & Mancktelow, N. S. (2007). Nucleation and initial growth of a shear zone network within compositionally and structurally heterogeneous granitoids under amphibolite facies conditions. *Journal of Structural Geology*, *29*(11), 1757–1780. https://doi.org/10.1016/j.jsg.2007.06.002

Piazolo, S., Daczko, N. R., Silva, D., & Raimondo, T. (2020). Melt-present shear zones enable intracontinental orogenesis. *Geology*. https://doi.org/10.1130/G47126.1

Popov, A. A., & Sobolev, S. V. (2008). SLIM3D: A tool for three-dimensional thermomechanical modeling of lithospheric deformation with elasto-visco-plastic rheology. *Physics of the Earth and Planetary Interiors*, *171*(1–4), 55–75. https://doi.org/10.1016/j.pepi.2008.03.007

Putnis, A. (2021). Fluid-Mineral Interactions: Controlling Coupled Mechanisms of Reaction, Mass Transfer and Deformation. *Journal of Petrology*, *62*(12), 1–27. https://doi.org/10.1093/petrology/egab092

Reber, J. E., Cooke, M. L., & Dooley, T. P. (2020). What model material to use? A Review on rock analogs for structural geology and tectonics. *Earth-Science Reviews*, *202*(September 2019), 103107. https://doi.org/10.1016/j.earscirev.2020.103107

Regenauer-Lieb, K., & Yuen, D. A. (2003). Modeling shear zones in geological and planetary sciences: Solid- and fluid-thermal-mechanical approaches. *Earth-Science Reviews*, *63*(3–4), 295–349. https://doi.org/10.1016/S0012-8252(03)00038-2

Rice, J. R. (1976). Localization of Plastic Deformation. *Theoretical and Applied Mechanics*, *1*, 207–220. https://doi.org/10.4028/www.scientific.net/ssp.3-4.347

Rogowitz, A., White, J. C., & Grasemann, B. (2016). Strain localization in ultramylonitic marbles by simultaneous activation of dislocation motion and grain boundary sliding (Syros, Greece). *Solid Earth*, *7*(2), 355–366. https://doi.org/10.5194/se-7-355-2016

Rolland, Y., Cox, S., Boullier, A. M., Pennacchioni, G., & Mancktelow, N. (2003). Rare earth and trace element mobility in mid-crustal shear zones: Insights from the Mont Blanc Massif (Western Alps). *Earth and Planetary Science Letters*, *214*(1–2), 203–219. https://doi.org/10.1016/S0012-821X(03)00372-8

Roy, A., Roy, N., Saha, P., & Mandal, N. (2021). Factors Determining Shear-Parallel Versus Low-Angle Shear Band Localization in Shear Deformations: Laboratory Experiments and Numerical Simulations. *Journal of Geophysical Research: Solid Earth*, *126*(10), 1–23. https://doi.org/10.1029/2021JB022578

Rudnicki, J. W. (1977). The Inception of Faulting in a Rock Mass With a Weakened Zone. *Journal of Geophysical Research*, *82*(5), 844–854.

Rudnicki, J. W., & Rice, J. R. (1975). Conditions for the localization of deformation in pressure-sensitive dilatant materials. *Journal of the Mechanics and Physics of Solids*, *23*(6), 371–394. https://doi.org/10.1016/0022-5096(75)90001-0

Rutter, E. H., Maddock, R. H., Hall, S. H., & White, S. H. (1986). Comparative microstructures of natural and experimentally produced clay-bearing fault gouges. *Pure and Applied Geophysics PAGEOPH*, *124*(1–2), 3–30. https://doi.org/10.1007/BF00875717

Sagapuram, D., Viswanathan, K., Trumble, K. P., & Chandrasekar, S. (2018). A common mechanism for evolution of single shear bands in large-strain deformation of metals. *Philosophical Magazine*, *98*(36), 3267–3299. https://doi.org/10.1080/14786435.2018.1524586

Scholz, C. H., & Choi, E. (2021). What comes first: The fault or the ductile shear zone? *Earth and Planetary Science Letters*, *577*, 117273. https://doi.org/10.1016/j.epsl.2021.117273

Snell, T., De Paola, N., van Hunen, J., Nielsen, S., & Collettini, C. (2020). Modelling fluid flow in complex natural fault zones: Implications for natural and human-induced earthquake nucleation. *Earth and Planetary Science Letters*, *530*, 115869. https://doi.org/10.1016/j.epsl.2019.115869

Snyder, D. B., & Kjarsgaard, B. A. (2013). Mantle roots of major precambrian shear zones inferred from structure of the great slave lake shear zone, northwest Canada. *Lithosphere*, *5*(6), 539–546. https://doi.org/10.1130/L299.1

Tvergaard, V., Needleman, A., & Lo, K. K. (1981). Flow localization in the plane strain tensile test. *Journal of the Mechanics and Physics of Solids*, *29*(2), 115–142. https://doi.org/10.1016/0022-5096(81)90019-3

Vauchez, A., Tommasi, A., & Mainprice, D. (2012). Faults (shear zones) in the Earth's mantle. *Tectonophysics*, *558–559*, 1–27. https://doi.org/10.1016/j.tecto.2012.06.006

Willis, K., Houseman, G. A., Evans, L., Wright, T., & Hooper, A. (2019). Strain localization by shear heating and the development of lithospheric shear zones. *Tectonophysics*, *764*(December 2018), 62–76. https://doi.org/10.1016/j.tecto.2019.05.010

Yuen, D. A., Fleitout, L., Schubert, G., & Froidevaux, C. (1978). Shear deformation zones along major transform faults and subducting slabs. *Geophysical Journal of the Royal Astronomical Society*, *54*(1), 93–119. https://doi.org/10.1111/j.1365-246X.1978.tb06758.x

Yuen, David A., & Schubert, G. (1977). ASTHENOSPHERIC SHEAR FLOW: THERMALLY STABLE OR UNSTABLE? *Geophysical Research Letters*, *4*(11).

Zielinski, P. G., & Ast, D. G. (1983). Slip bands in metallic glasses. *Philosophical Magazine A: Physics of Condensed Matter, Structure, Defects and Mechanical Properties*, *48*(5), 811–824. https://doi.org/10.1080/01418618308236546

Figure captions:

Figure 1: a) Schematic presentation of the deformation zig used for compression tests under plane strain condition. The orientations of the principal stress axes are shown in the corresponding panel. b) A perspective view of heterogeneous PS model, containing two through-going cylindrical weak flaws with their axes perpendicular to the principal compression direction (σ_1-axis) and aligned along the direction of no strain (σ_2-axis). The PS block was allowed to extend in the horizontal direction (σ_3-axis) at right angle to the flaw axis. (c) Stress versus strain

746 relations for homogeneous and heterogeneous PS models obtained from laboratory experiments
747 at low (2 x 10^{-5} sec^{-1}) and high (3 X 10^{-5} sec^{-1}) strain rates.

748

749 Figure 2: Shear band growth in PS model experiments with increasing finite strain. a) Uniform
750 development of closely spaced, conjugate narrow bands (NBs) in homogenous PS models
751 deformed at high strain rate ($\dot{\varepsilon} = 3 \text{ X } 10^{-5}\ sec^{-1}$). Note at higher finite strain, shear zone forms
752 at a high angle to the compression direction, marked by dotted red line. b) Formation of wide
753 composite bands (CBs) preferentially against the weak flaws in a heterogeneous PS model at a
754 high strain rate. The composite structure consists of a core and a transition zone, dominated by
755 band-parallel and orthogonal NBs. c) Formation of homogeneously sheared bands (HBs),
756 bordered by narrow zones of gradational shear contacts with the weakly strained walls. The
757 heterogeneous PS model was deformed at a low strain rate (2 x 10^{-5} sec^{-1}). The photographs are
758 obtained from thin sections of deformed PS blocks observed under cross polarized light.

759

760 Figure 3: a) Band density mapping (Estimated Density (P20), mm^{-2}), b) histogram and c) rose
761 diagrams of band orientations for i) homogenous PS models and ii) PS models containing
762 cylindrical weak flaws. Note that the band density plots show a clear transition of distributed
763 NBs in homogenous model to localized CBs in a PS model with weak flaws, where the band core
764 regions have the highest band concentrations.

765

766 Figure 4: Structural characteristics of the three types of shear bands in PS models (thin sections
767 under cross polars). a) Uniformly distributed NBs in homogeneous PS deformed at high $\dot{\varepsilon}$ (3 x
768 10^{-5} sec^{-1}). Note that the bands define conjugate orientations (white dotted lines) with dihedral
769 angle (Φ) of ~85°-88° b) Composite band (CB) in a PS block containing weak flaws deformed at
770 high $\dot{\varepsilon}$ (3 x 10^{-5} sec^{-1}). The CB structure is composed of a core zone (cluster of finely spaced
771 parallel narrow bands), bounded by transition zone (marked by green color), containing a
772 dominant set of orthogonal NBs. The red lines show the accommodated viscous drag in the
773 transition zone. The core zone generally forms at a low angle (~ 10°-15°) to the overall CB trend.
774 c) Homogeneous shear band (HB) in a PS block with weak flaws deformed at low $\dot{\varepsilon}$ (2 x 10^{-5} sec^{-}

[1]) Note that the band shows a wide core zone of homogeneous internal shear strain, and a narrow zone of gradational shear, as revealed from optical birefringence.

Figure 5: a) Initial finite element (FE) model setup used for numerical experiments (details provided in Table S1). The circle (yellow) at the center represents a weak flow in the FE model domain. Arrows indicate the kinematic boundary conditions imposed at the model boundaries. b) 1D rheological representation of the FE modelling. This decomposition can be interpreted as Maxwell visco-elasto-plastic rheology, where plastic, viscous and elastic components are connected in series. σ_e, η_v, and G: plastic yield stress, material viscosity and shear modulus of the material, respectively. c) Stress versus strain relations obtained from progressive deformations of visco-elasto-plastic numerical models. Note that the model with an initial weak flaw yields at a lower stress than a homogenous model (free from any initial flaw).

Figure 6: Progressive development of shear bands in a) a homogeneous model and b) a heterogeneous model with an initial weak flaw, deformed at high strain rates (3×10^{-5} sec^{-1}), and c) a similar heterogeneous model, but deformed under a relatively low strain rate (2×10^{-5} sec^{-1}). The color bar represents the magnitude of strain rate 2nd invariant. The finite model shortening is indicated at the top of each panel. Note that the core zones (red regions) in bands produced in the heterogeneous model under high strain rates (b) form at an angle (~7°-10°) to the overall band trend, as in the laboratory models (Fig 2b-iii)

Figure 7: Across-band strain profiles in deformed numerical models (locations of the profile lines: AB, CD, and EF, shown in Fig 6 ai). The profiles reveal systematic variations of the 2nd invariant strain rate tensor, where the peaks demarcate the locations of shear band localization in a homogeneous and a heterogeneous model simulation: MS1 and MS3.

Figure 8: Field photographs of outcrop-scale shear zones in the Chotonagpur Granite Gneissic Complex (CGGC), Eastern India showing a) Narrow shear Bands (NBs), b) Composite shear Bands (CBs) and c) Homogenous shear Bands (HBs). a-i) Multiple narrow shear zones of conjugate orientations (NBs) distributed in a single ~ 100 m x 50 m outcrop of homogeneous

quartzo-feldspathic rocks. a-ii) A single NB (3mm thickness) in an outcrop of banded gneiss. b-i) Heterogeneity (quartzo-feldspathic aggregates) controlled localization of composite shear bands in conjugate sets, radiating from the heterogeneity. Each band shows a core of strongly sheared rocks, flanked by foliation drag zones. b-ii) A single CB formed along an inherent heterogeneity with prominent drag zone and strongly sheared core. c-i) and ii) Shear zones containing a wide band of homogeneous shear strain (core), bordered by narrow zones of relatively weak shear, grading into unsheared wall rocks.

Figure 9: a-i) High-resolution structural map (1:100) of a homogeneous quartzo-feldspathic outcrop showing spatially distributed numerous NBs (marked by red color) in conjugate sets. a-ii) Corresponding histogram and (a-iii) rose diagram of the shear band orientations shown in the map. b) Construction of across-band strain profiles based on field measurements: i) Type I, ii) Type II and iii) Type III shear zones.

Figure 1.

a

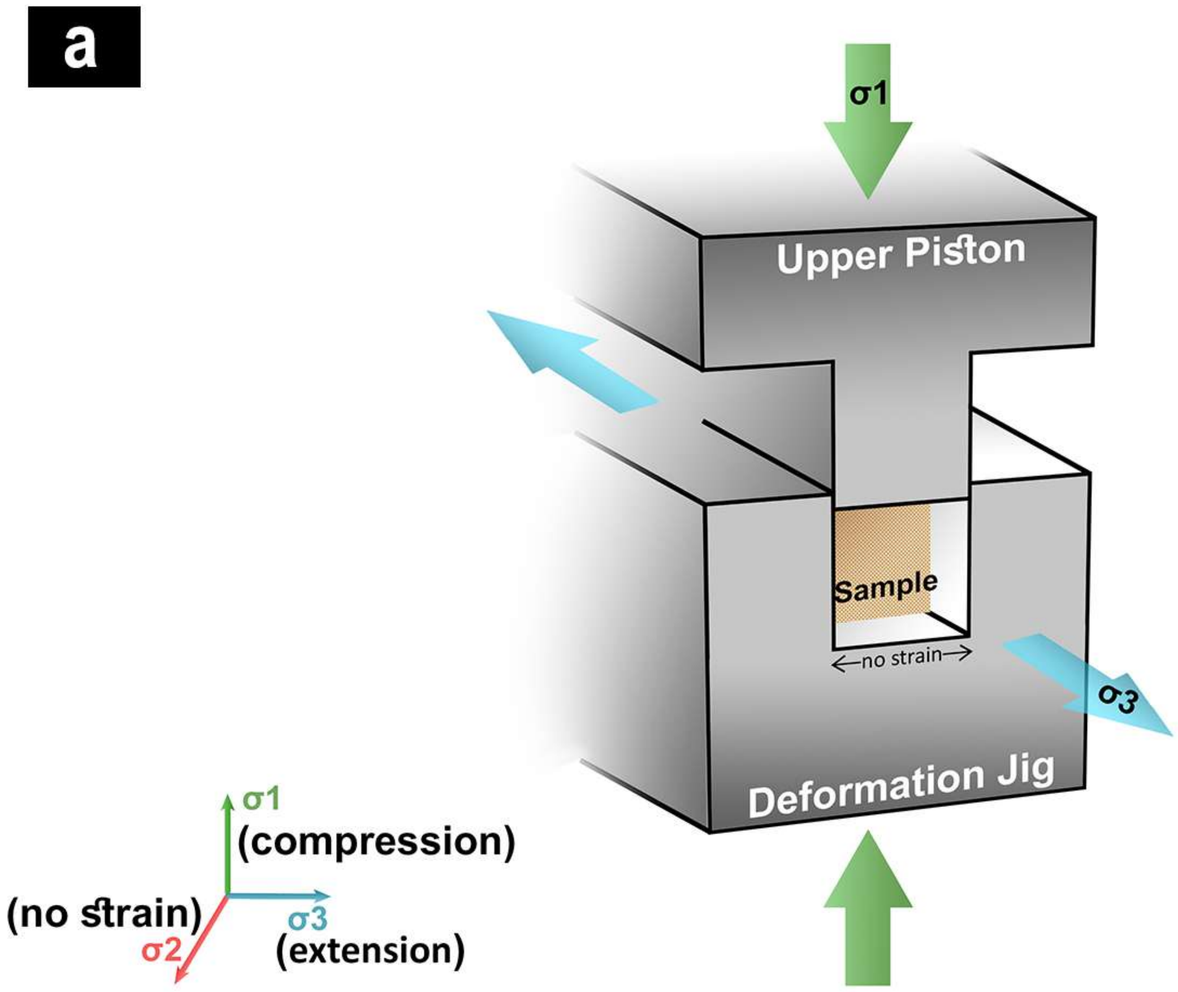
σ1
Upper Piston
Sample
no strain
σ3
Deformation Jig
σ1
(compression)
(no strain)
σ2
σ3
(extension)

b

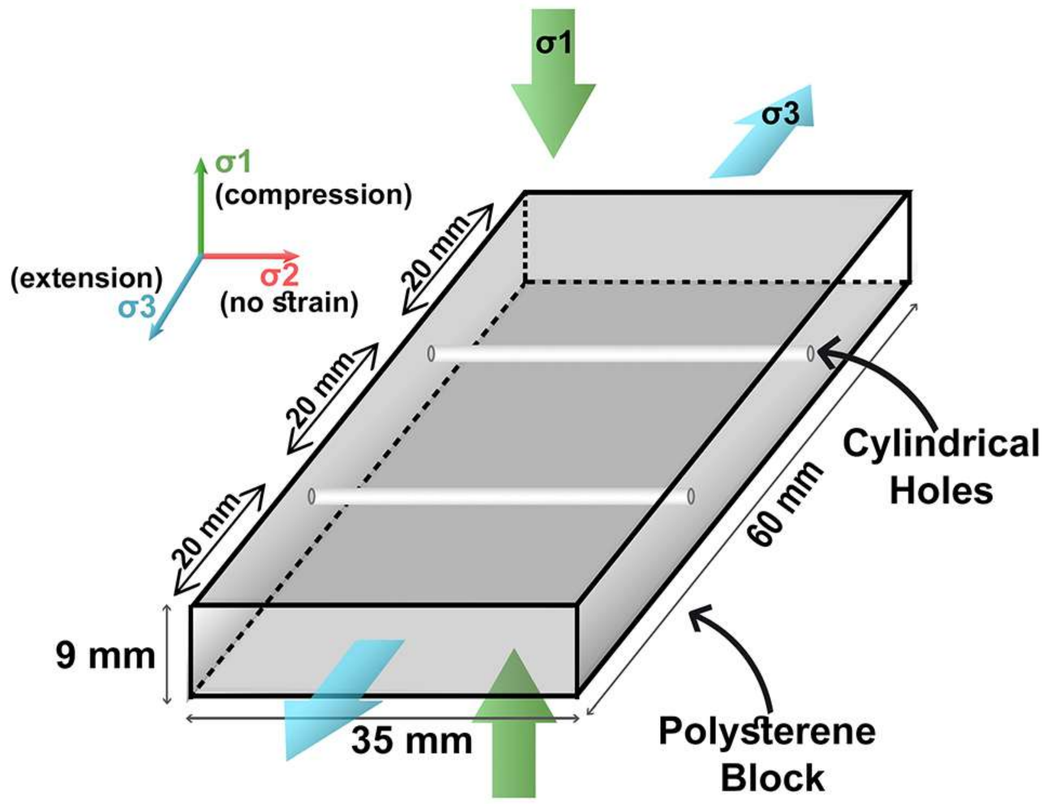
σ1
σ3
σ1
(compression)
(extension)
σ3
σ2
(no strain)
20 mm
20 mm
20 mm
Cylindrical
Holes
60 mm
9 mm
35 mm
Polysterene
Block

c

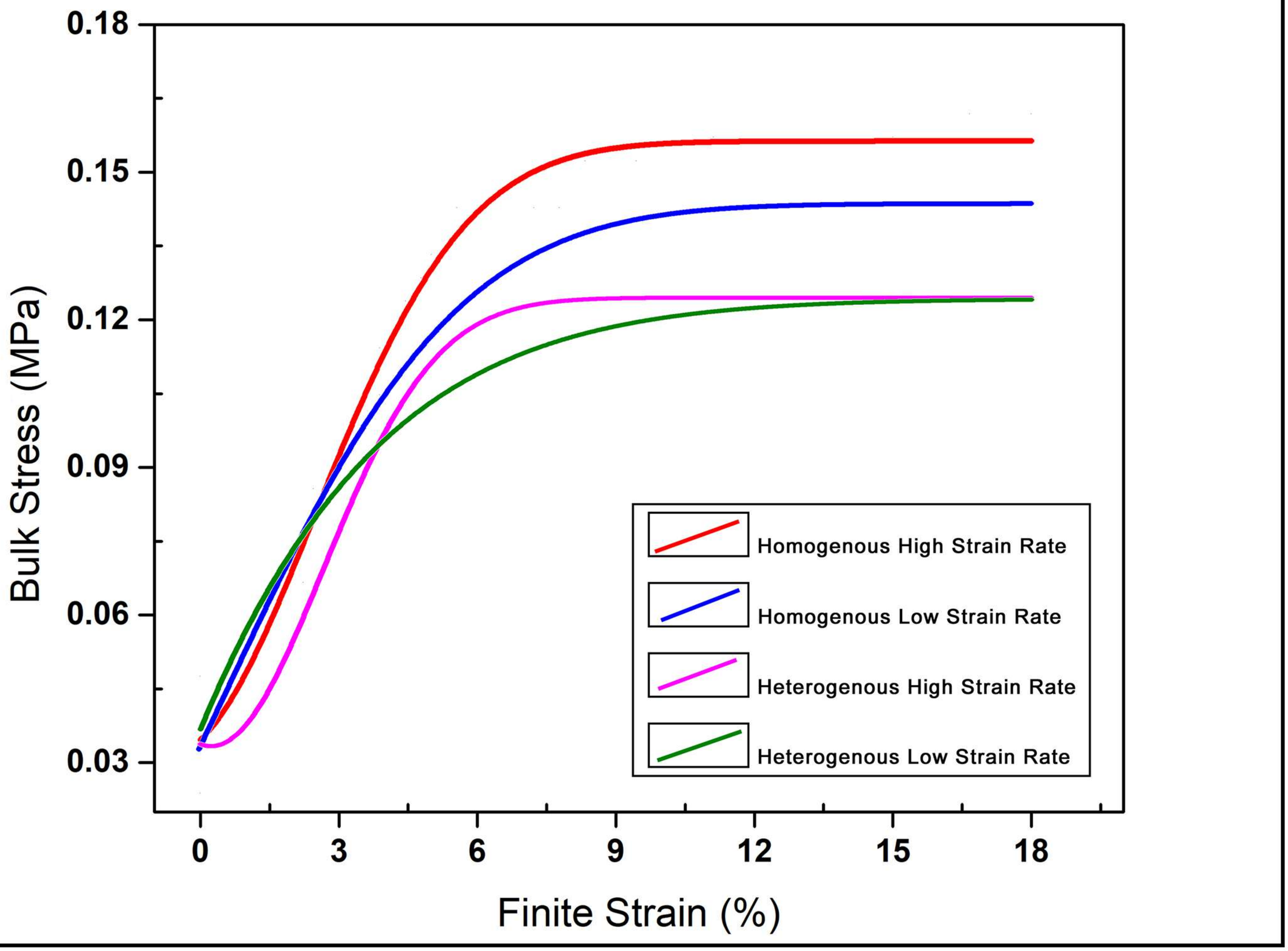
0.18
0.15
0.12
0.09
0.06
0.03
Bulk Stress (MPa)
0
3
6
9
12
15
18
Finite Strain (%)
Homogenous High Strain Rate
Homogenous Low Strain Rate
Heterogenous High Strain Rate
Heterogenous Low Strain Rate

Figure 2.

a

b

c

Finite Strain

6%

12%

18%

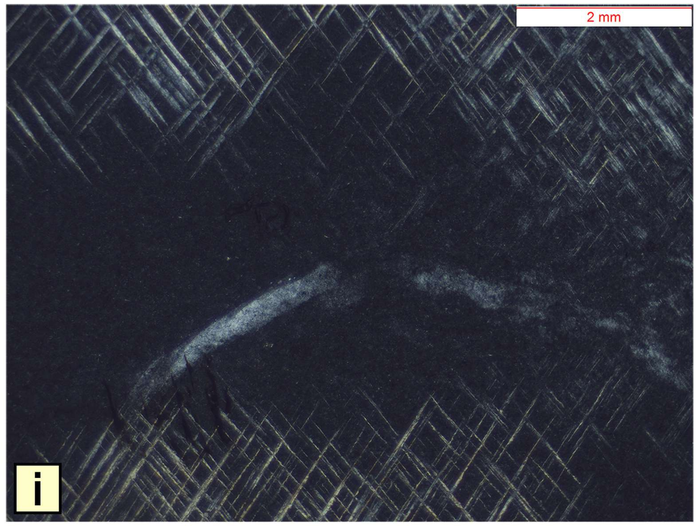

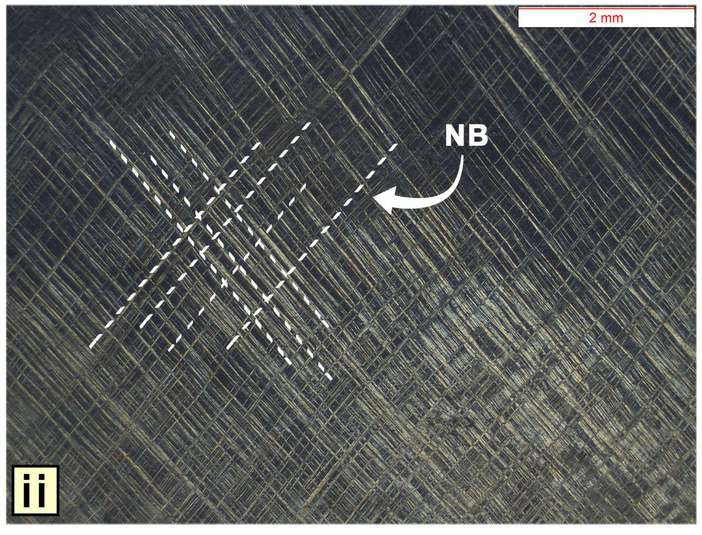

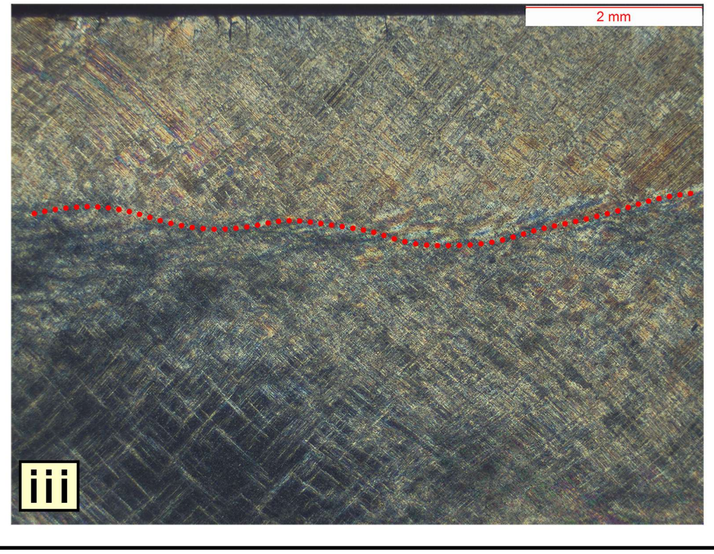

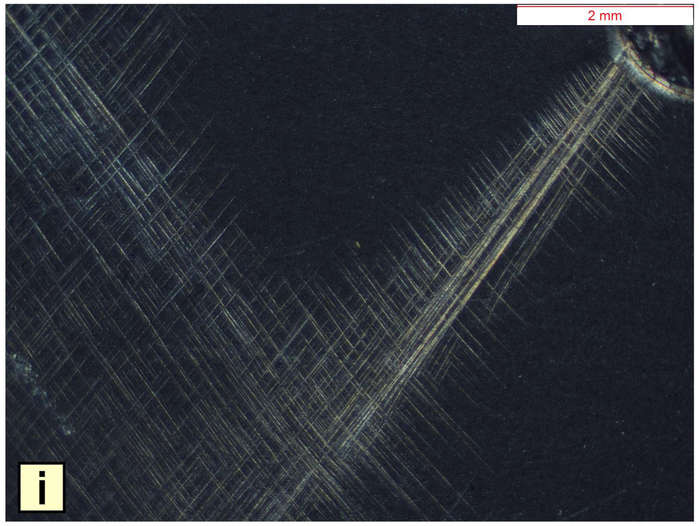

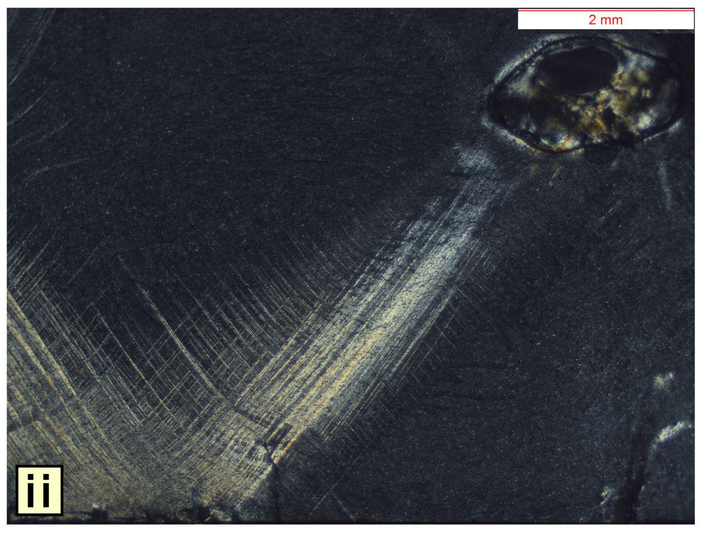

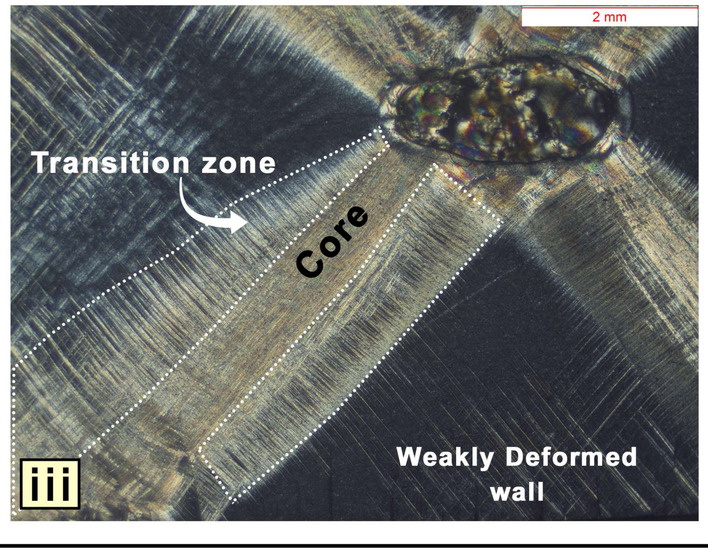

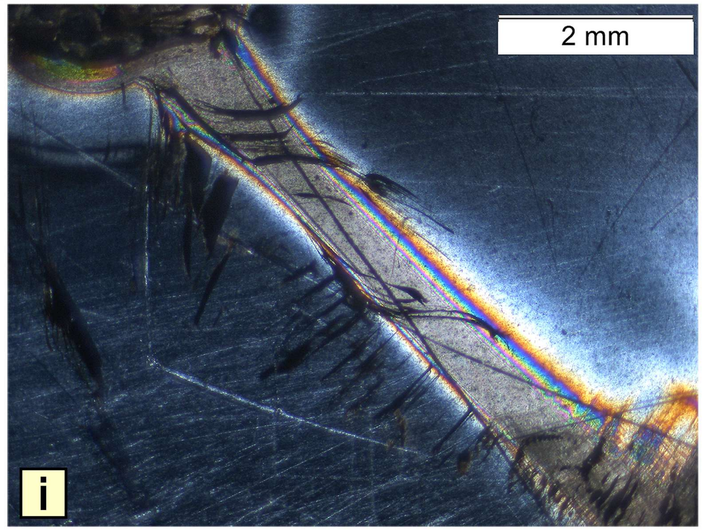

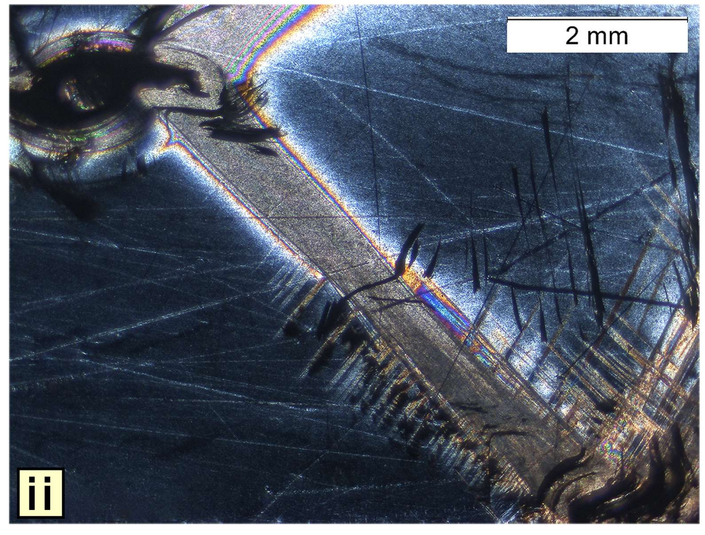

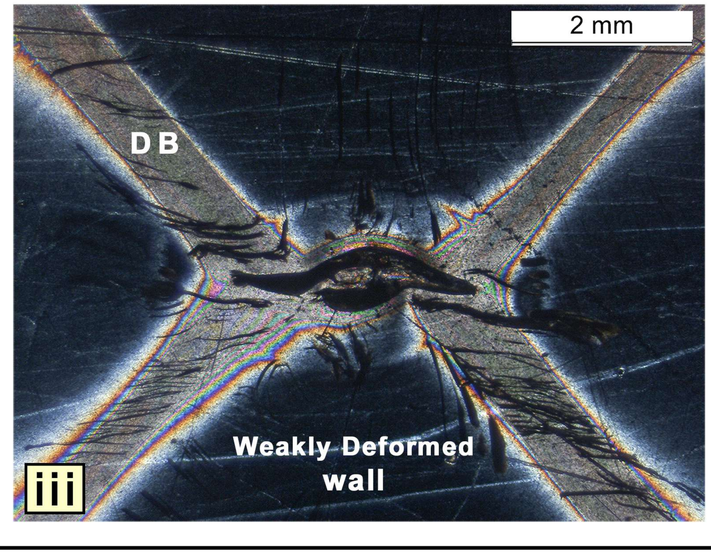

Figure 3.

a

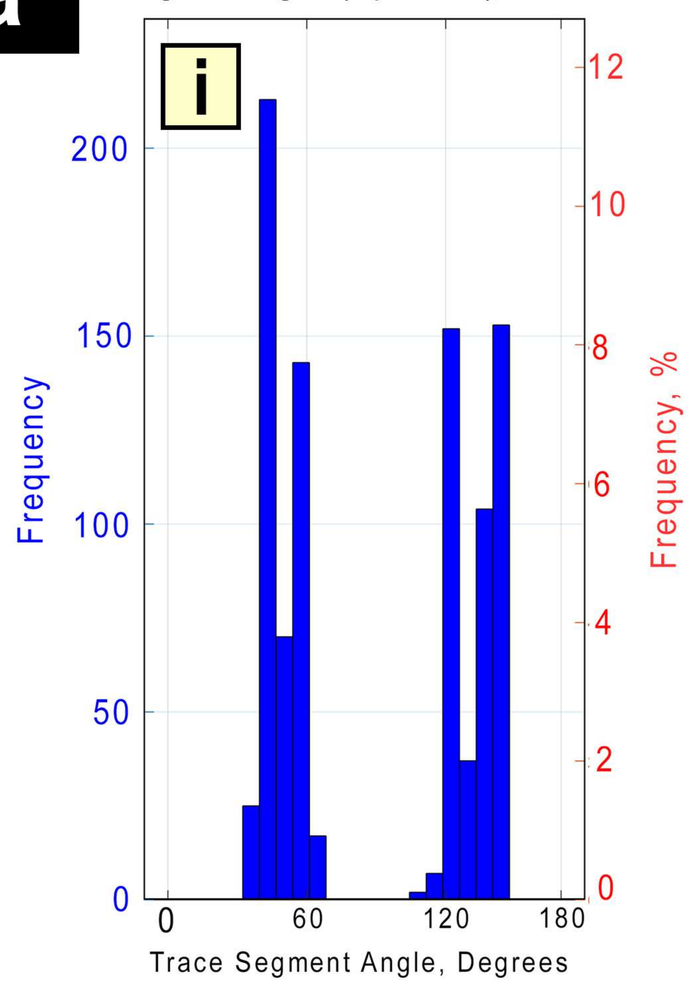
Segment angles (equal area), n = 923
i
Frequency
Frequency, %
0
50
100
150
200
0
2
4
6
8
10
12
0
60
120
180
Trace Segment Angle, Degrees

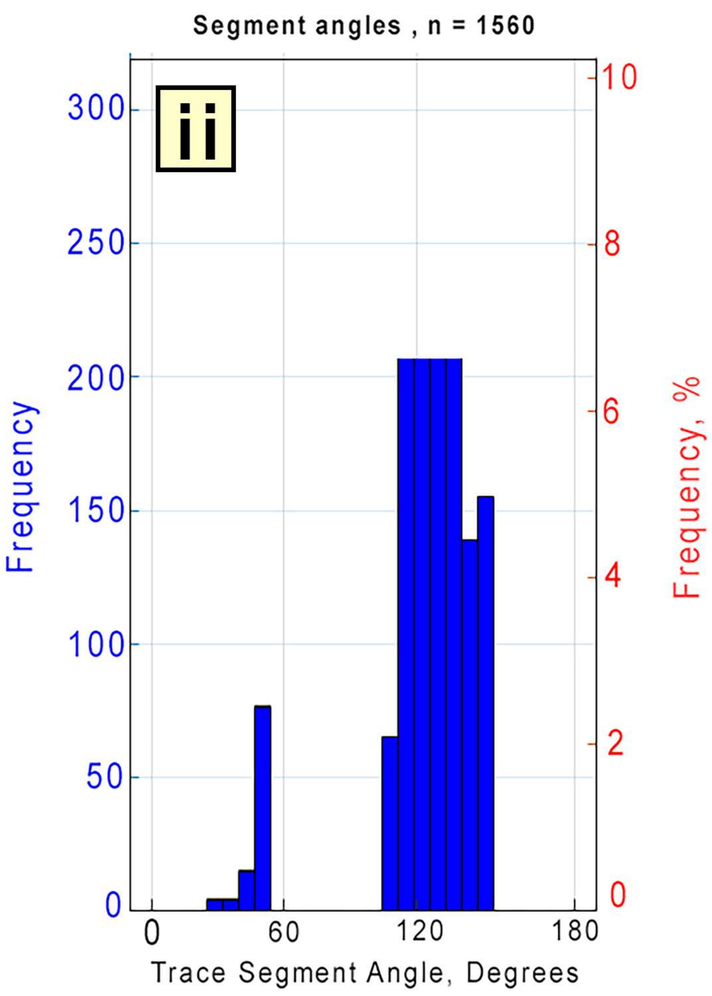
Segment angles , n = 1560
ii
Frequency
Frequency, %
0
50
100
150
200
250
300
0
2
4
6
8
10
0
60
120
180
Trace Segment Angle, Degrees

c

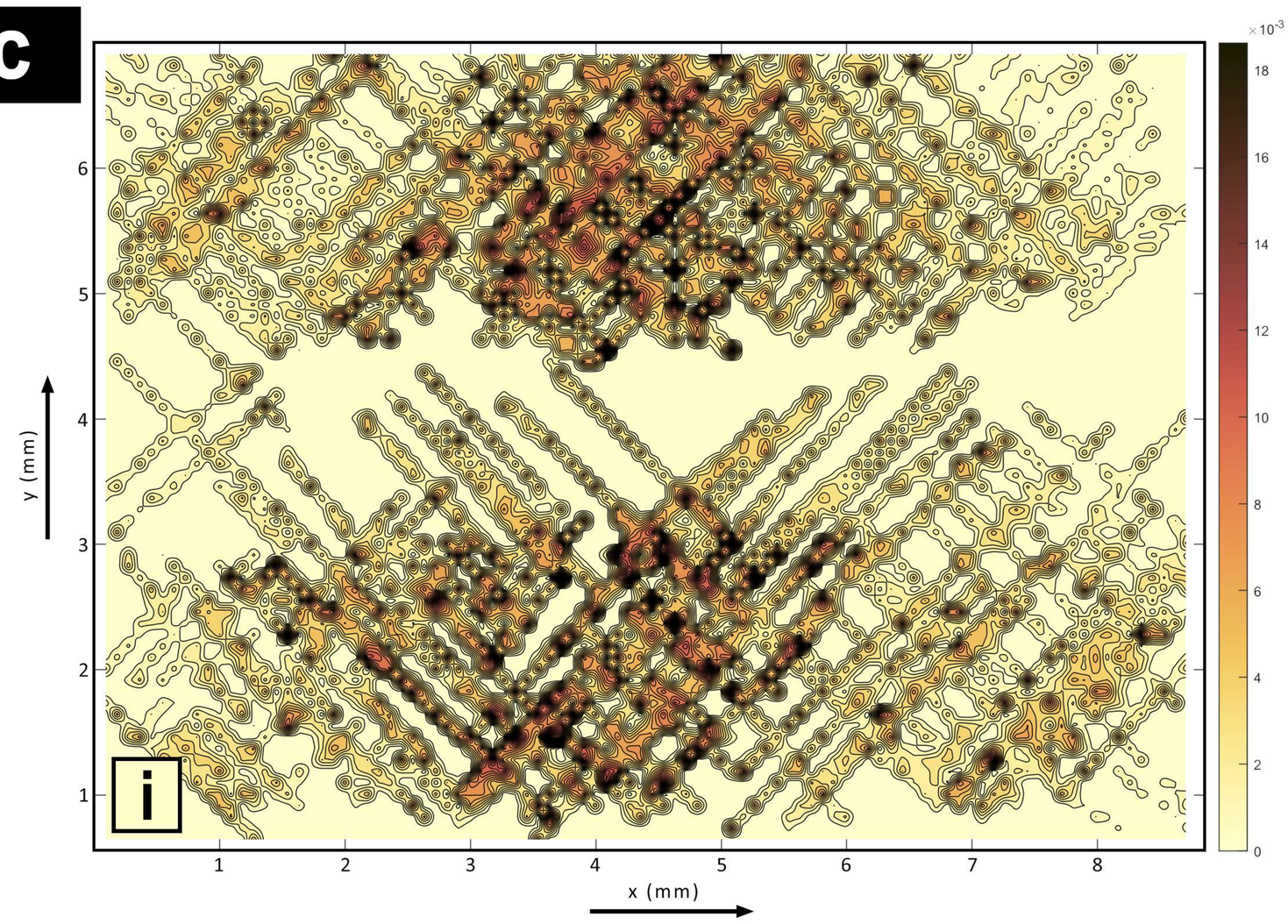
i
y (mm)
x (mm)
1
2
3
4
5
6
7
8
×10-3
0
2
4
6
8
10
12
14
16
18

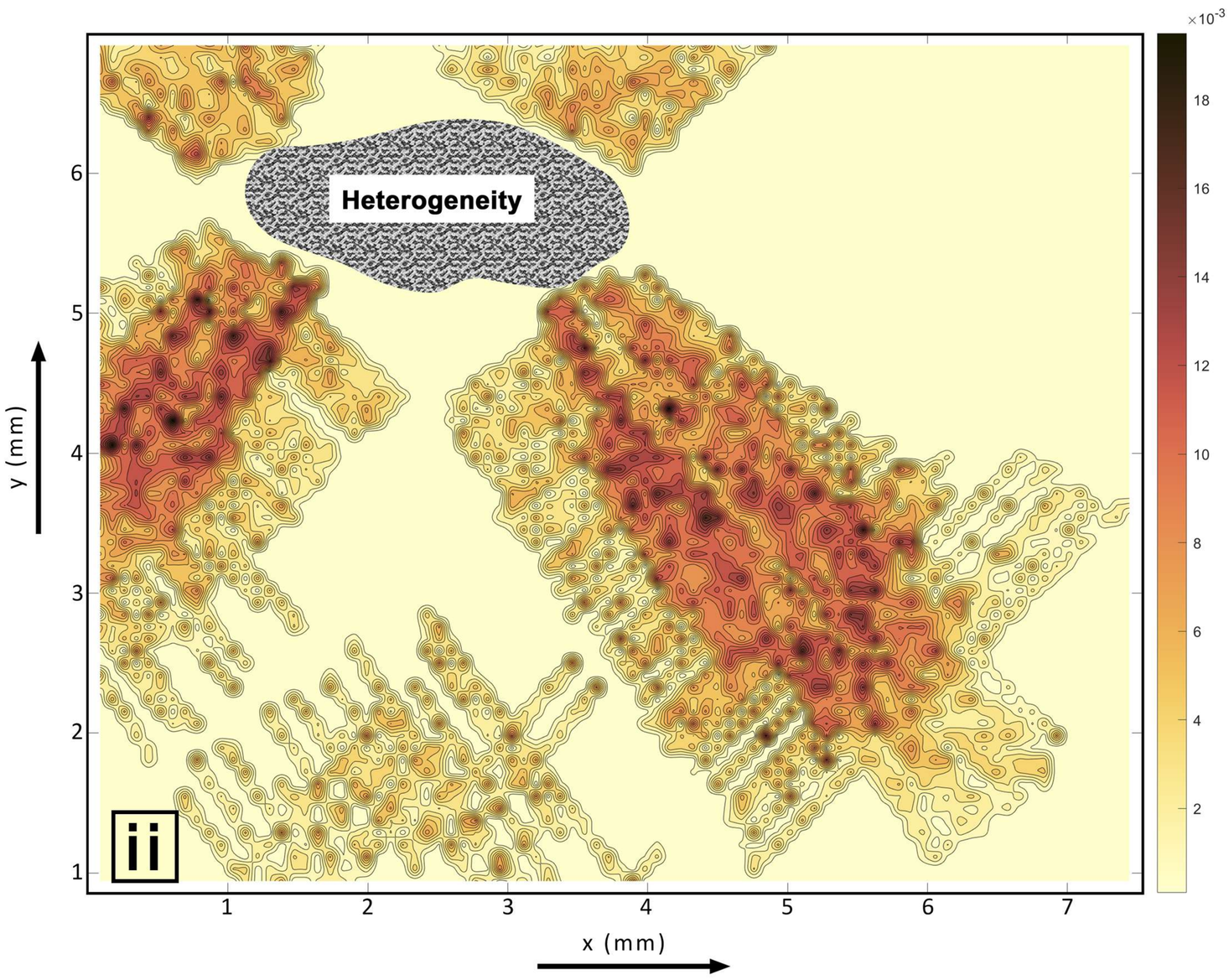
Heterogeneity
ii
y (mm)
x (mm)
1
2
3
4
5
6
7
×10-3
2
4
6
8
10
12
14
16
18

b

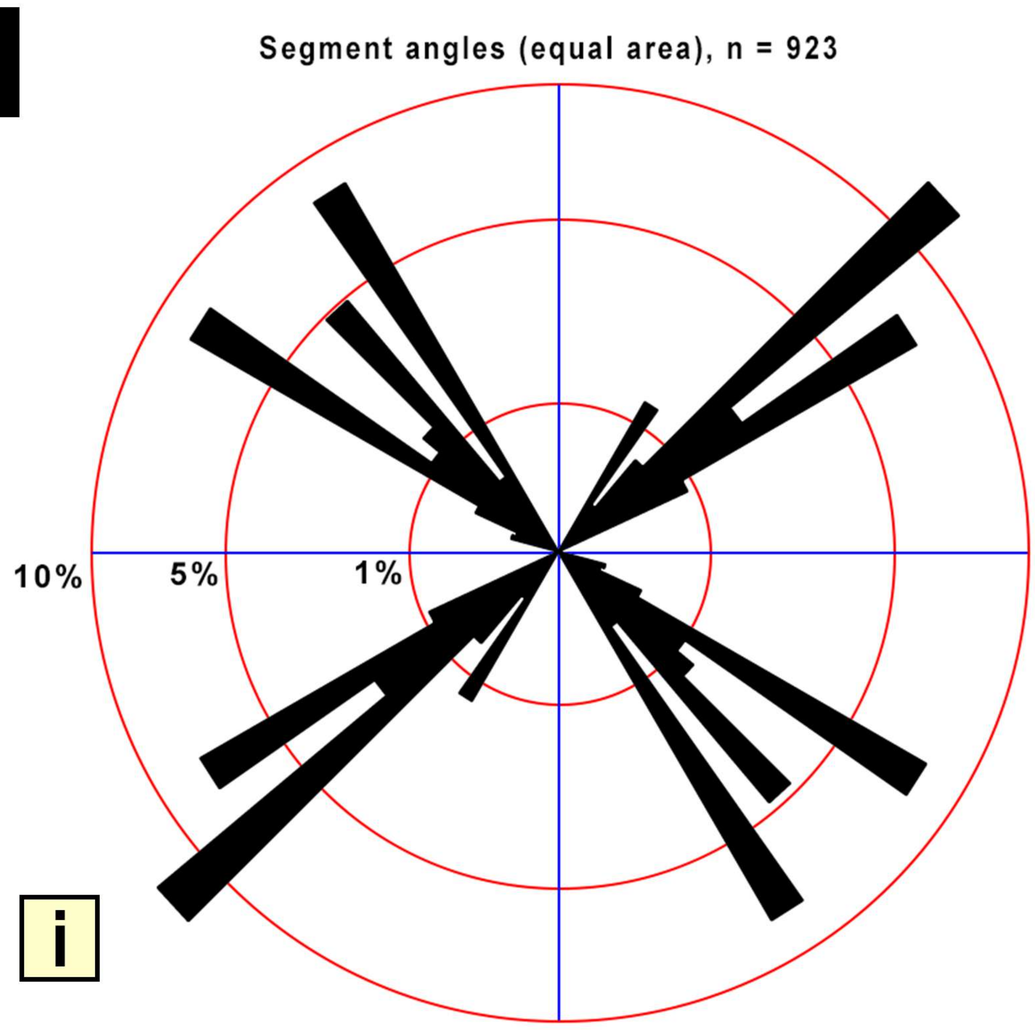
Segment angles (equal area), n = 923
10%
5%
1%
i

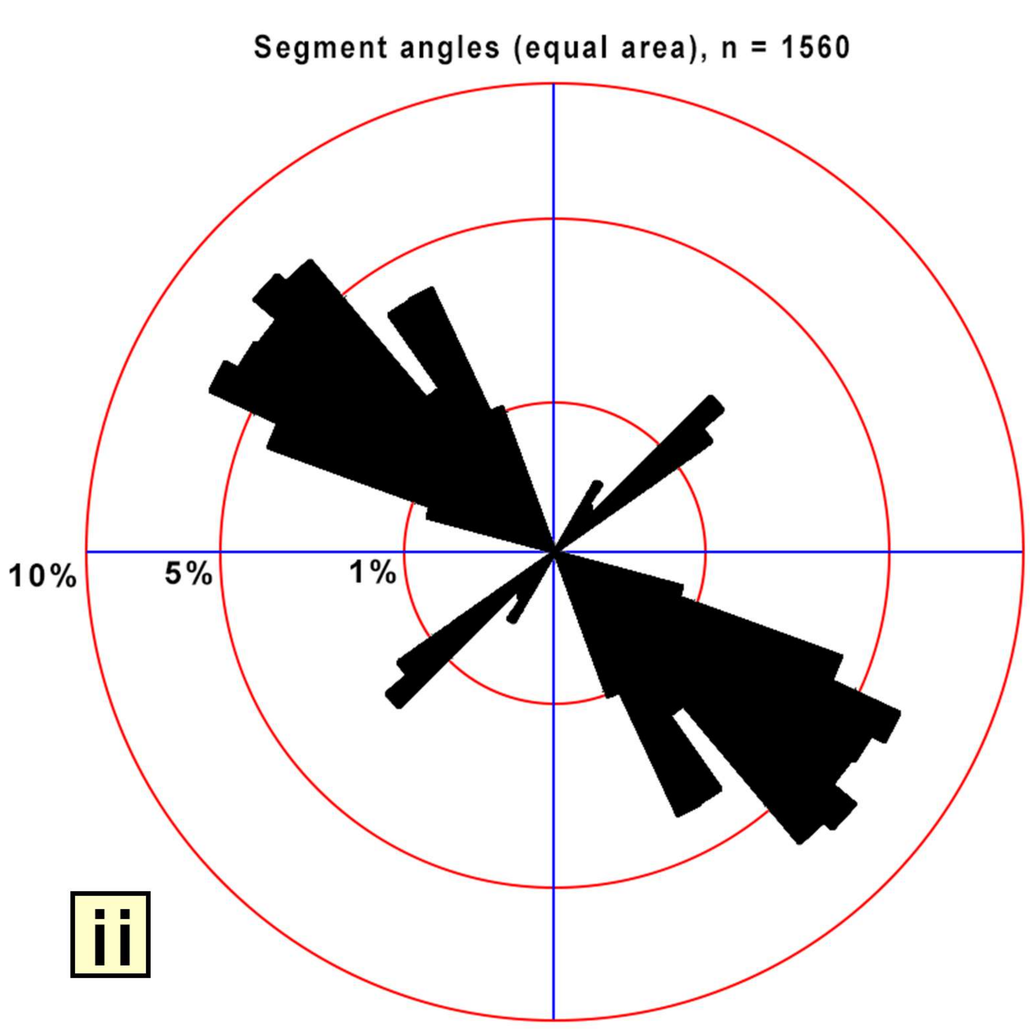
Segment angles (equal area), n = 1560
10%
5%
1%
ii

Figure 4.

a

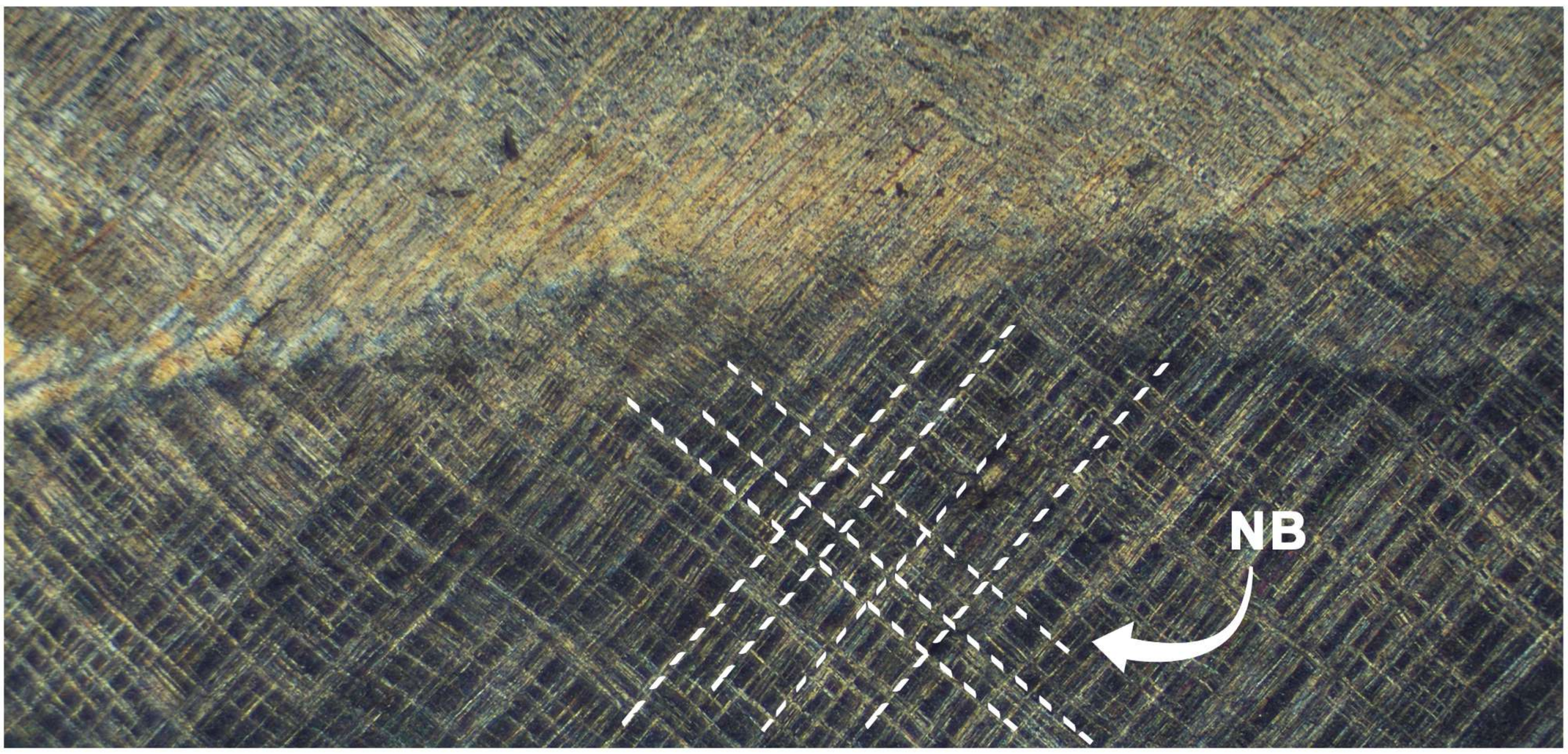
NB

b

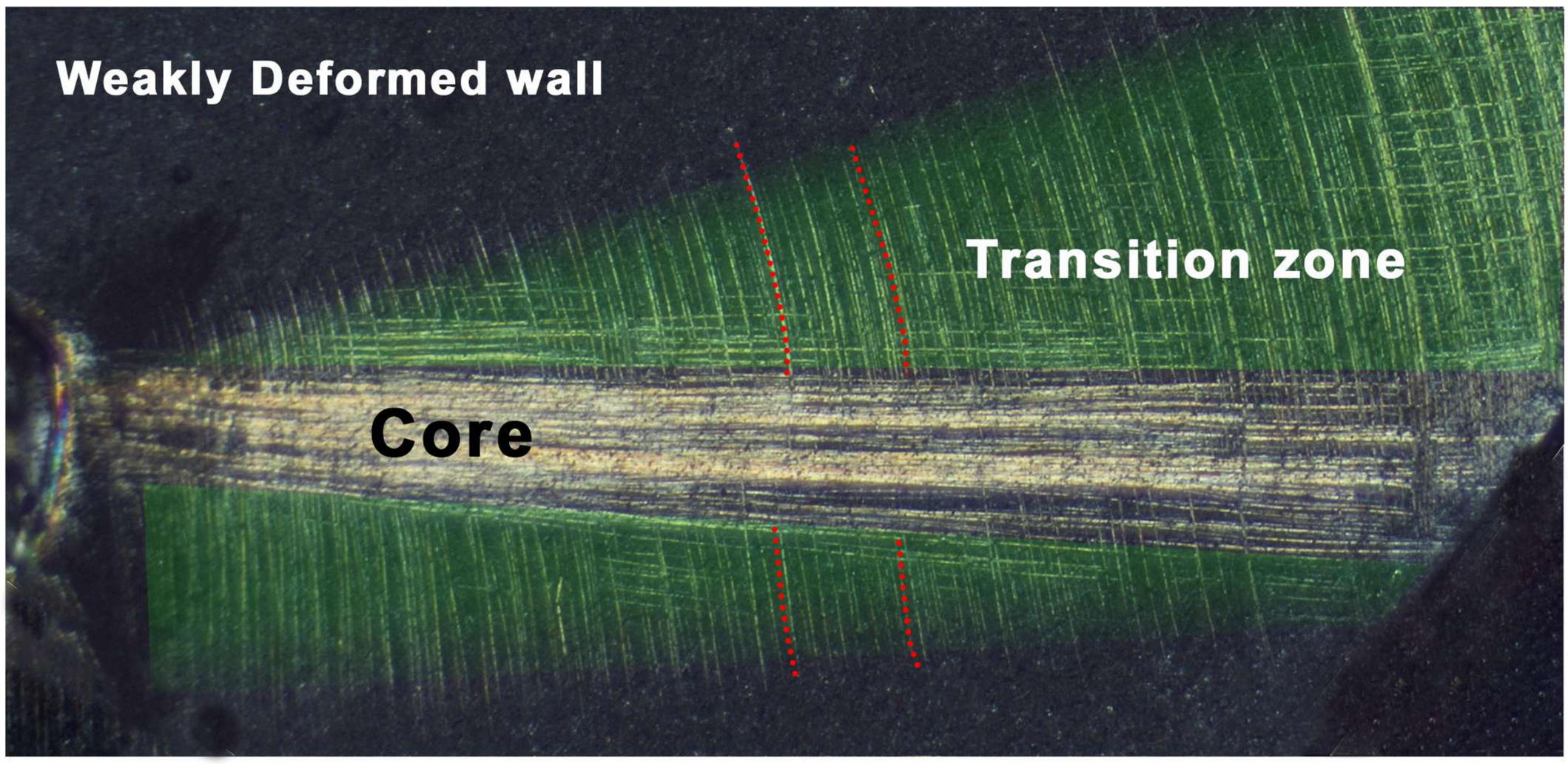
Weakly Deformed wall
Transition zone
Core

C

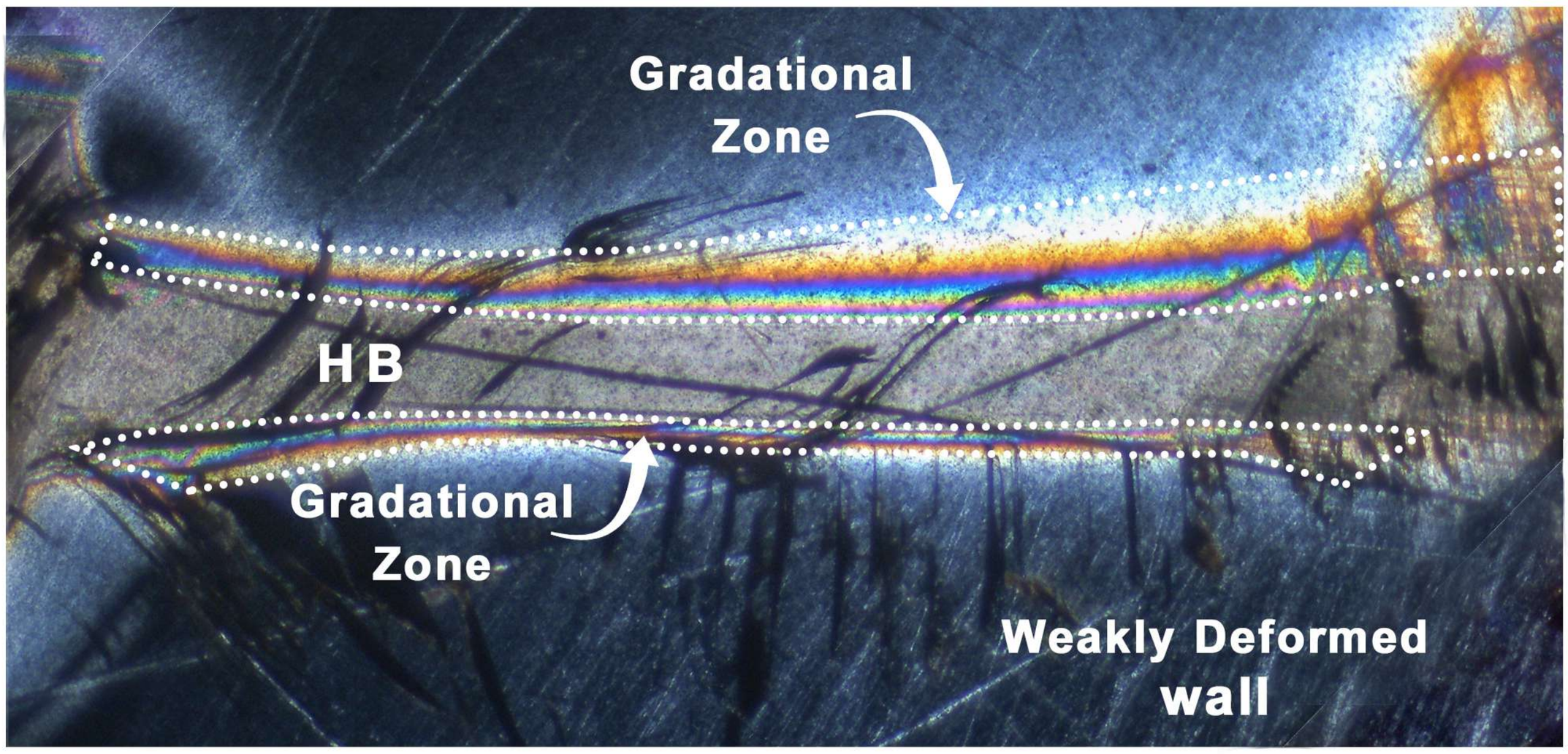
Gradational Zone
HB
Gradational Zone
Weakly Deformed wall

Figure 5.

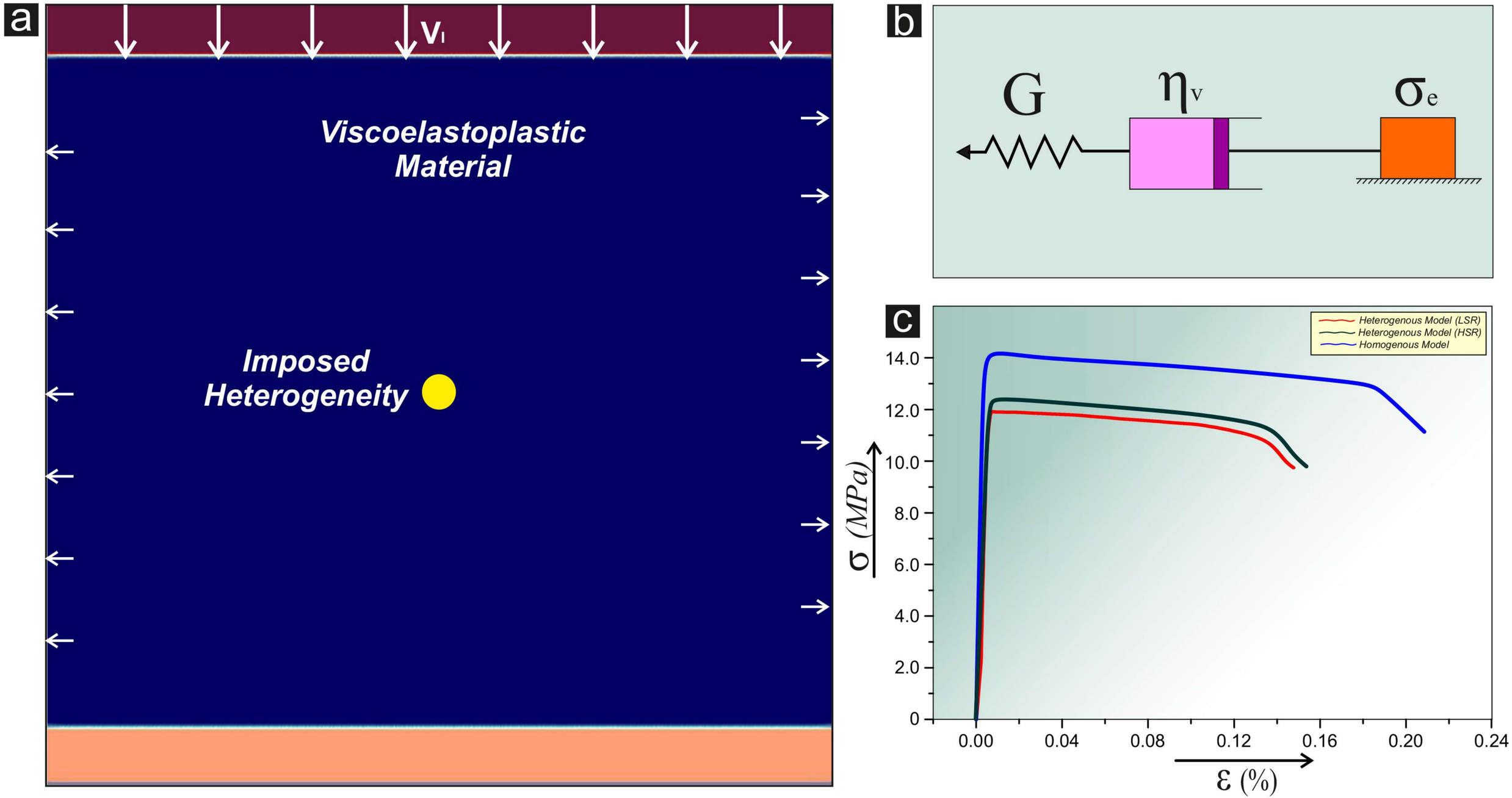
a
V_l
Viscoelastoplastic Material
Imposed Heterogeneity
b
G
η_v
σ_e
c
Heterogenous Model (LSR)
Heterogenous Model (HSR)
Homogenous Model
σ (MPa)
ε (%)
0
2.0
4.0
6.0
8.0
10.0
12.0
14.0
0.00
0.04
0.08
0.12
0.16
0.20
0.24

Figure 6.

5%

10%

15%

20%

a No Pre-existing Flaw

A

B

C

D

E

F

i

ii

iii

iv

0

25

50

b Pre-existing Flaw (HSR)

i

ii

iii

iv

0

25

50

c Pre-existing Flaw

i

ii

iii

iv

0

5

10

Figure 7.

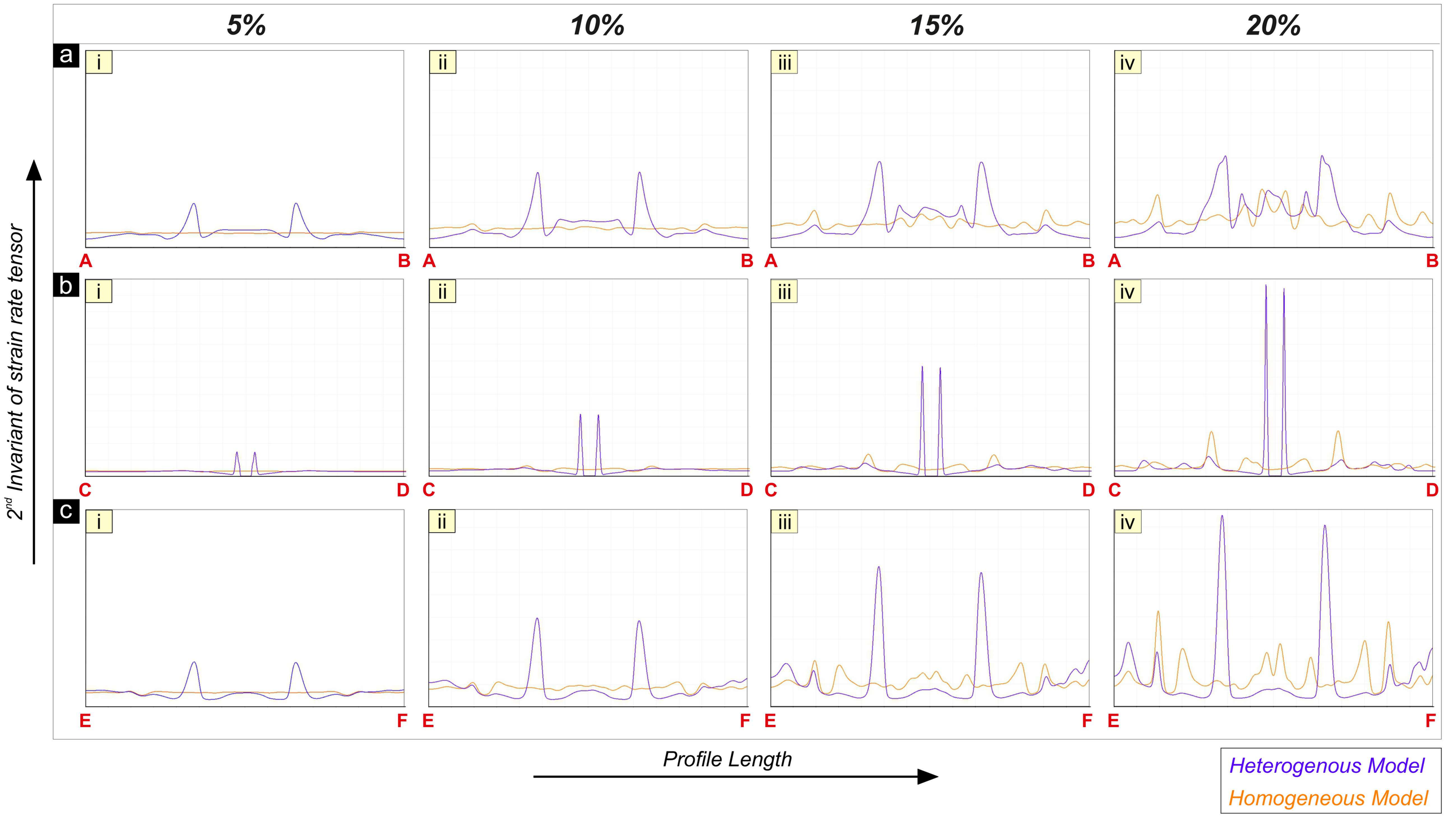
5%
10%
15%
20%
a
b
c
i
ii
iii
iv
A
B
C
D
E
F
2nd Invariant of strain rate tensor
Profile Length
Heterogenous Model
Homogeneous Model

Figure 8.

a

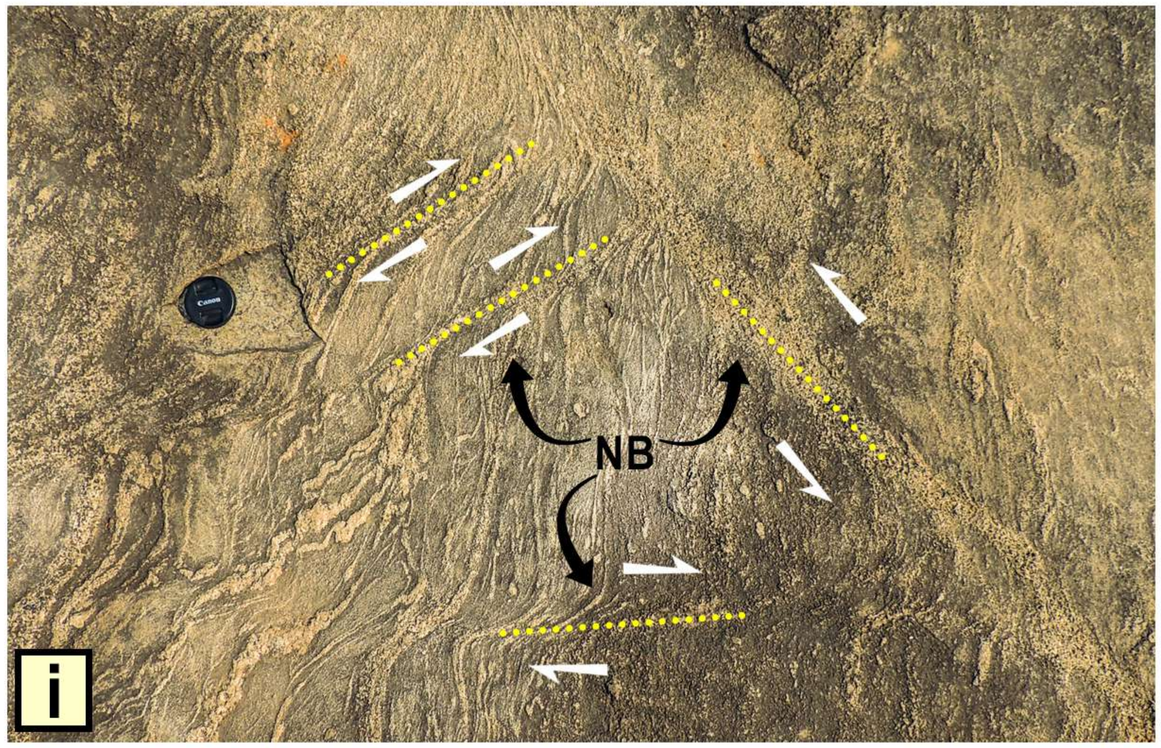

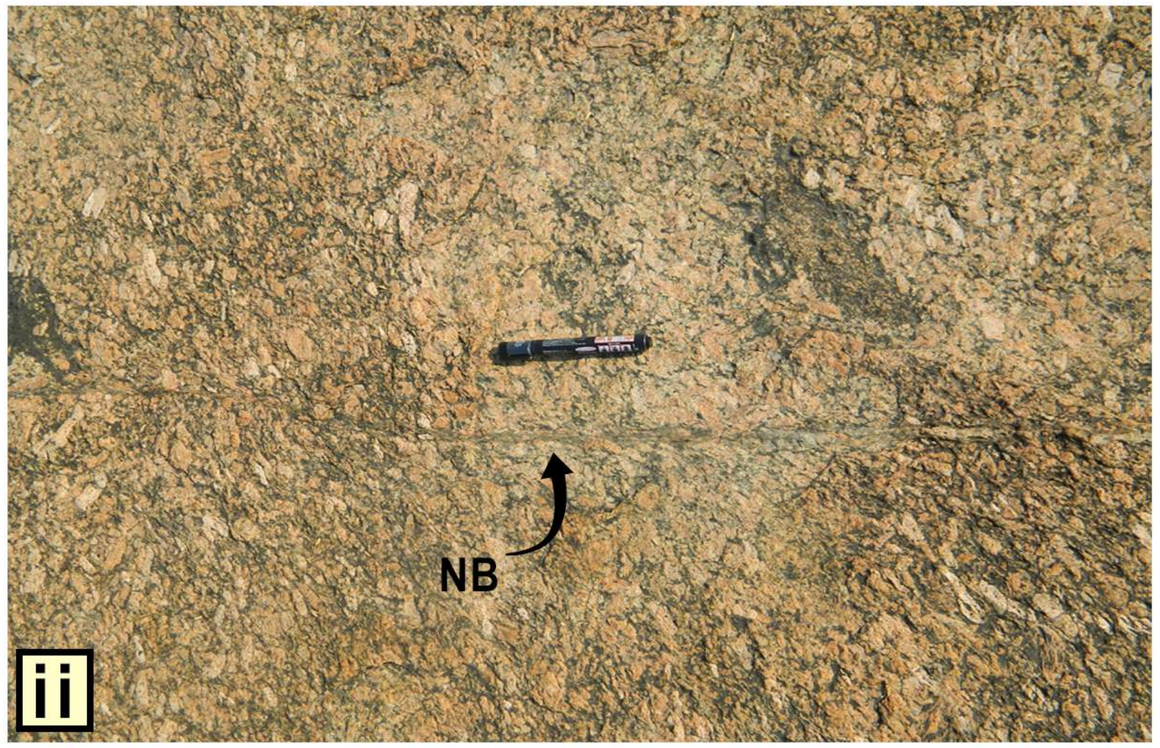

b

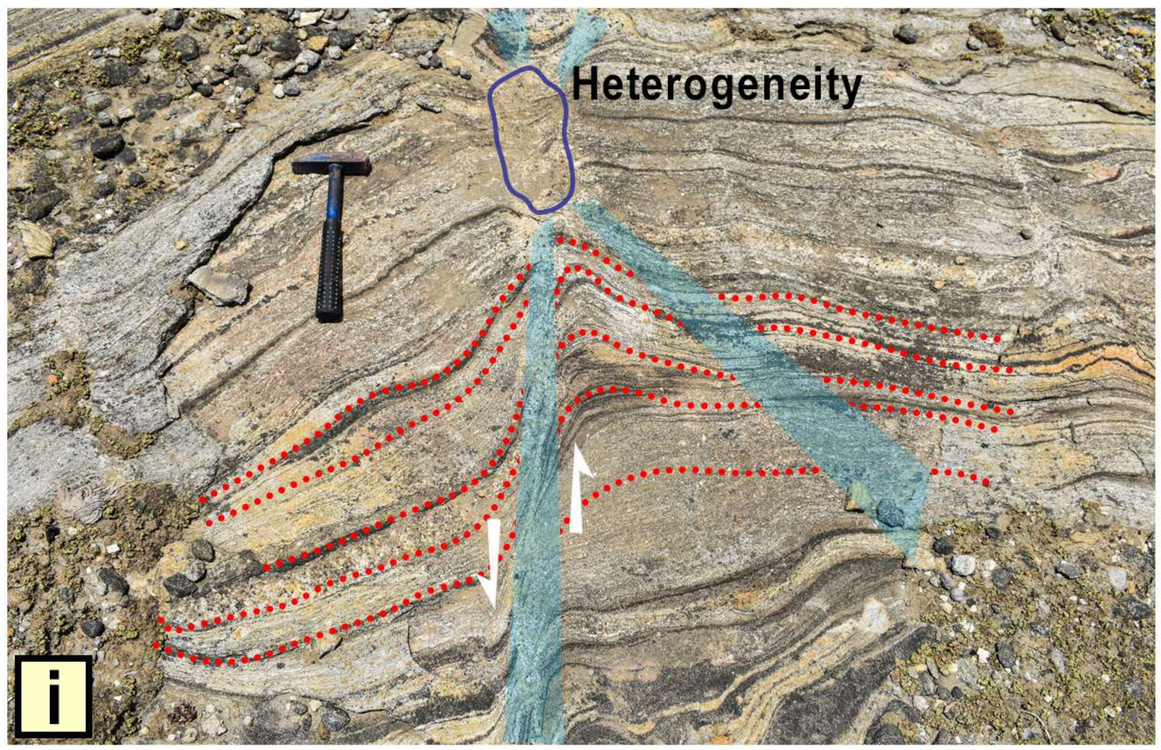

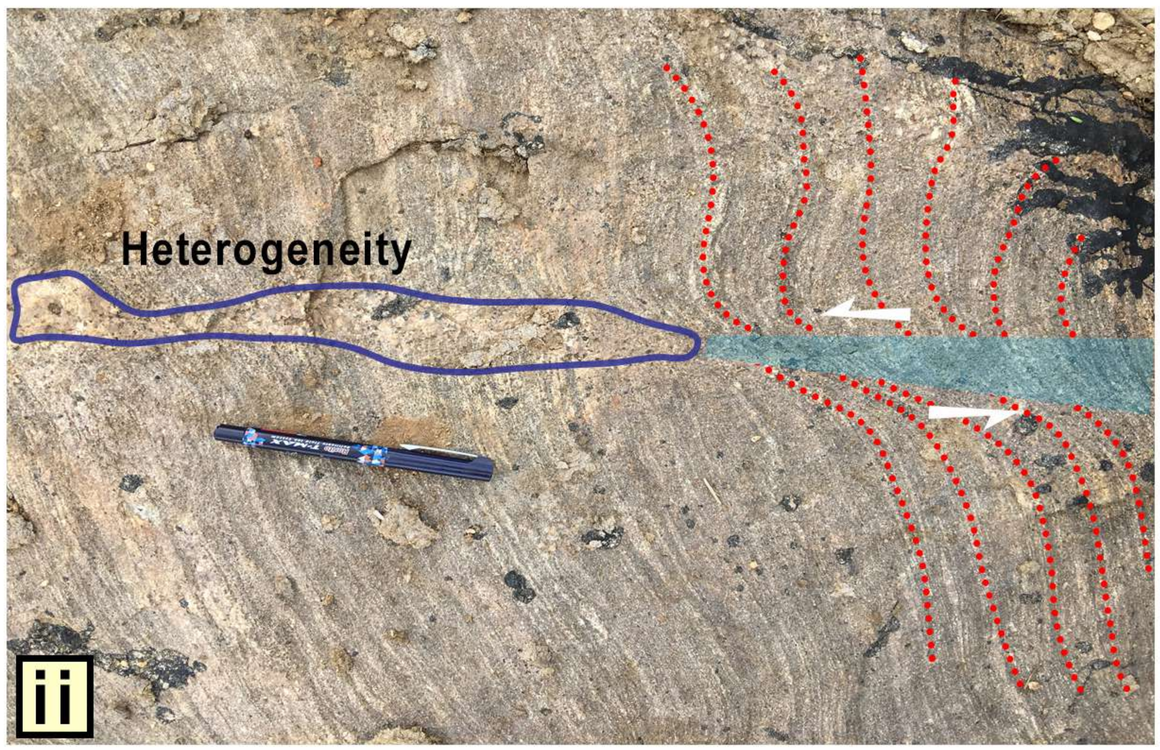

c

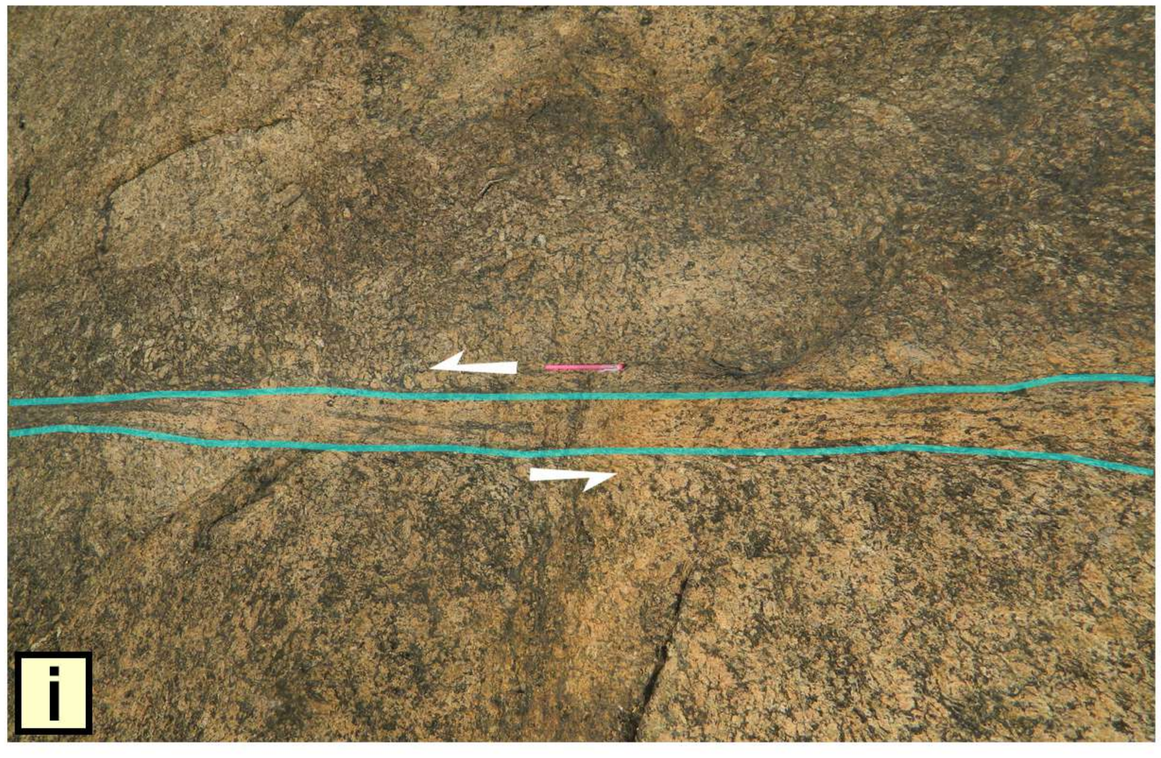

Figure 9.

a

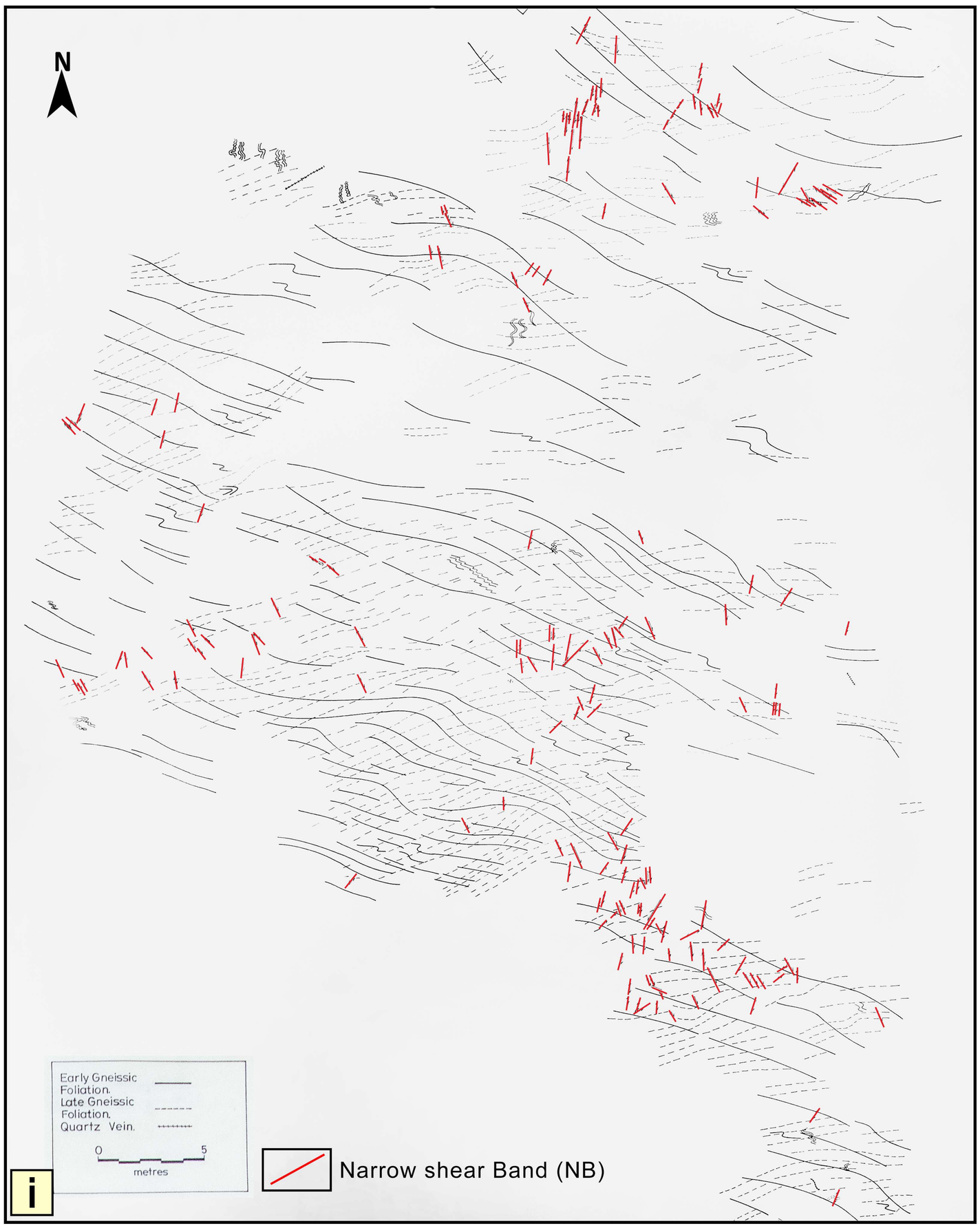
N
Early Gneissic Foliation.
Late Gneissic Foliation.
Quartz Vein.
0
5
metres
i
Narrow shear Band (NB)

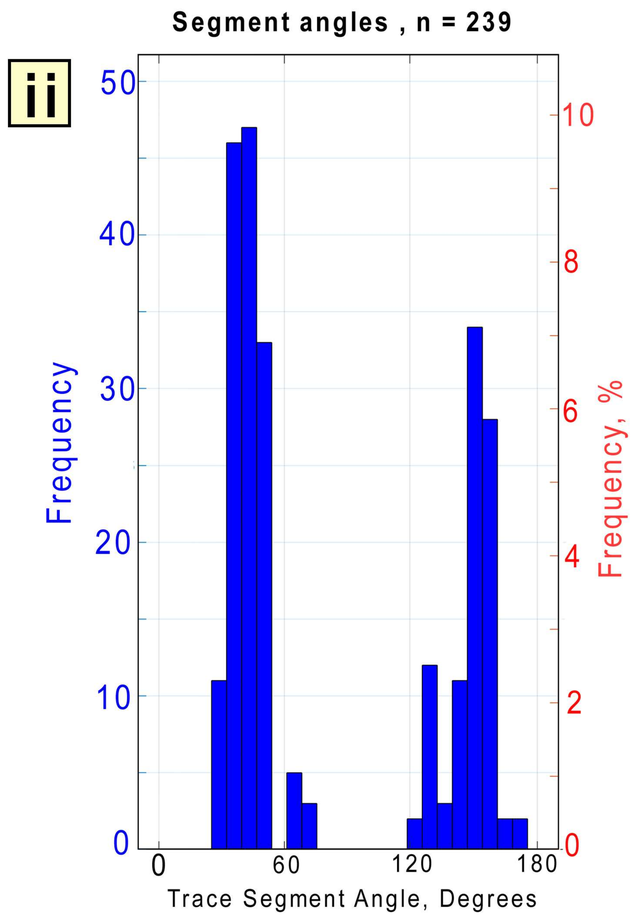
Segment angles , n = 239
ii
Frequency
Frequency, %
0
10
20
30
40
50
0
2
4
6
8
10
0
60
120
180
Trace Segment Angle, Degrees

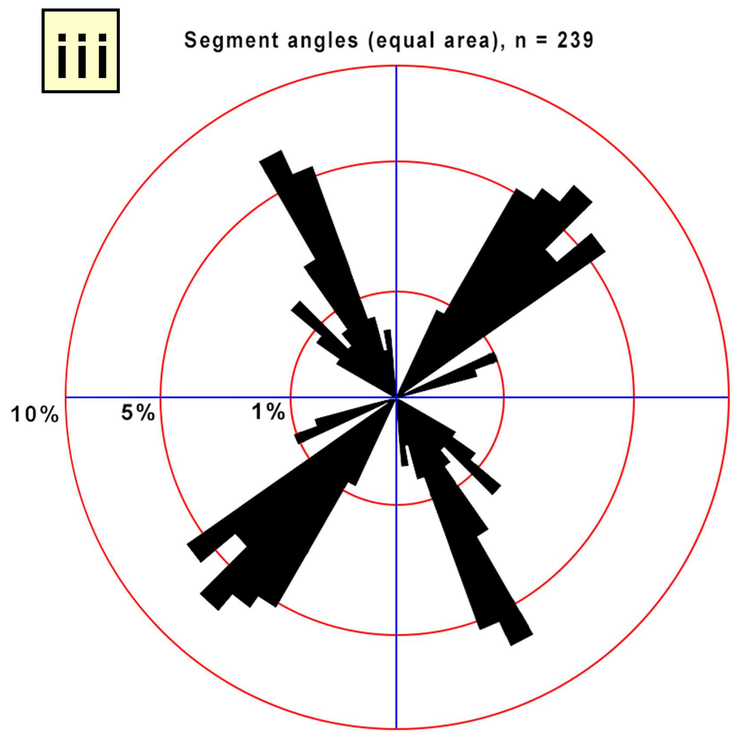
iii
Segment angles (equal area), n = 239
10%
5%
1%

b

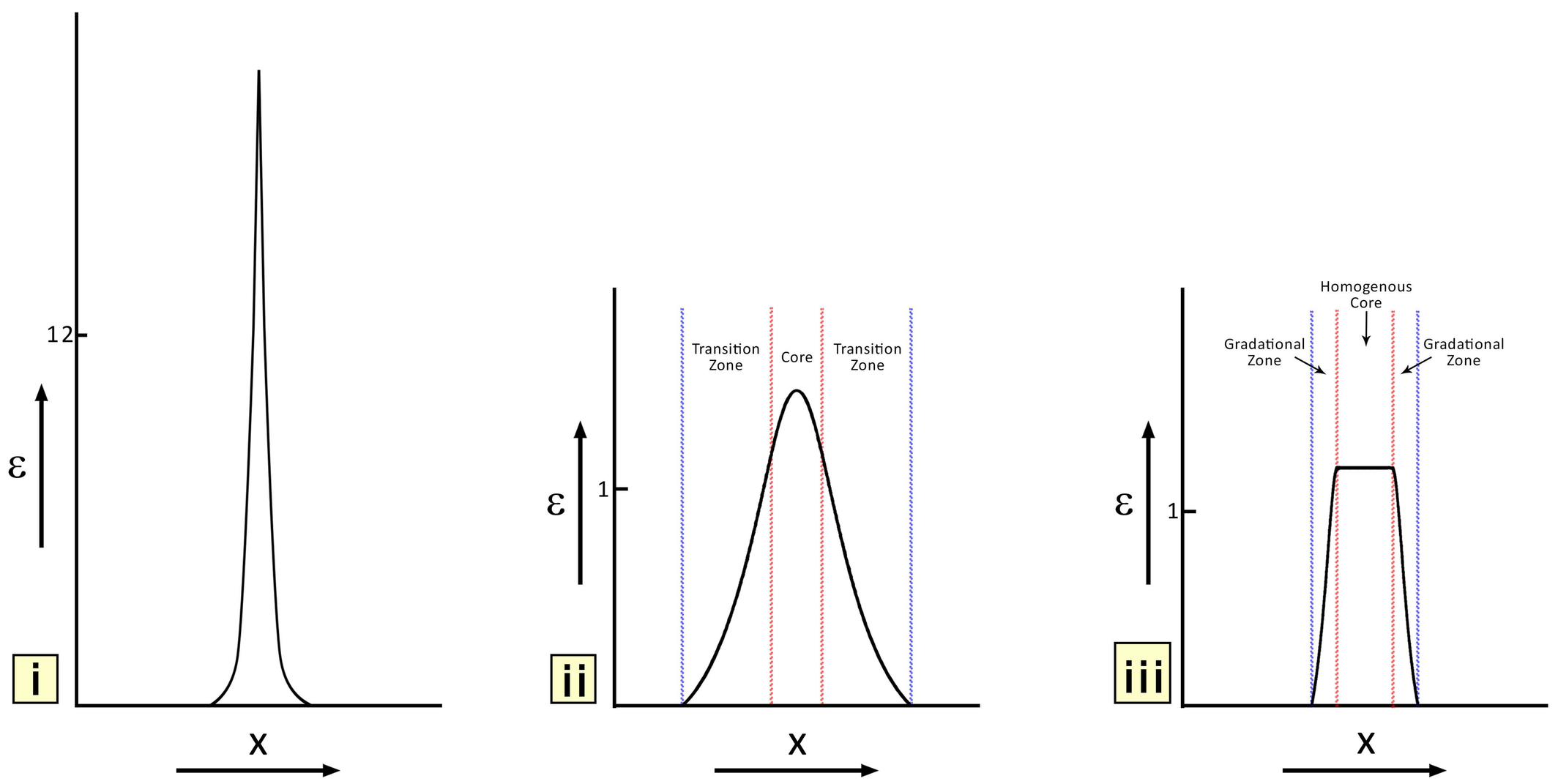
12
ε
i
X
Transition Zone
Core
Transition Zone
1
ε
ii
X
Homogenous Core
Gradational Zone
Gradational Zone
1
ε
iii
X

Journal of Geophysical Research: Solid Earth

Supporting Information for

Mechanisms of shear band formation in heterogeneous materials under compression: The role of pre-existing mechanical flaws

Manaska Mukhopadhyay, Arnab Roy and Nibir Mandal*

High Pressure and Temperature Laboratory, Department of Geological Sciences, Jadavpur University, Kolkata 700032, India.

Contents of this file

S1. Homogeneous model experiments at lower strain rate

We performed an additional set of experiments to test the sensitivity of homogenous PS blocks to strain rate in forming shear band structures (Fig S1). The experiments were run at a lower strain rate, 3×10^{-5} sec^{-1} to 2×10^{-5} sec^{-1}, as compared to those presented in the main text (Fig 2a). This range of strain rates produced sharp and narrow bands that are finely spaced and uniformly distributed in the entire model. They typically formed in conjugate sets, symmetrically oriented with respect to the compression

direction. The bands multiplied in number with increasing finite strain, as observed in similar experiments at relatively higher rates, and they had no tendency to widen, but grow in length. The PS produced distributed narrow bands in its homogeneous state under the entire range of strain rate conditions used in our laboratory experiments. We thus conclude that uniformly thick bands of homogeneous shear (HBs) in low-strain rate experiments reflect the influence of weak flaws in the model.

Figure S1: Uniform development of closely spaced, conjugate narrow bands (NBs) in homogenous PS models deformed at low strain rate ($\dot{\varepsilon} = 2 \times 10^{-5}\ sec^{-1}$). Note that strain rate doesn't have any effect on shear band formation in homogeneous model.

S2. Across-band strain profiles in numerical models

This section discusses the strain profiles calculated from the numerical simulation MS2 run at relatively high rates (results presented in the main text). The profiles are

constructed along the lines AB, CD, EF, as shown in Figure 6 in the main text. They represent plots of the 2nd invariant of the strain rate tensor (sum of the elastic, viscous and plastic strain components) as a function of distance in the model. The strain profiles contain multiple peaks that reveal the composite nature of shear bands, as observed in the PS experiments at a high strain rate ($3 \times 10^{-5}\ sec^{-1}$).

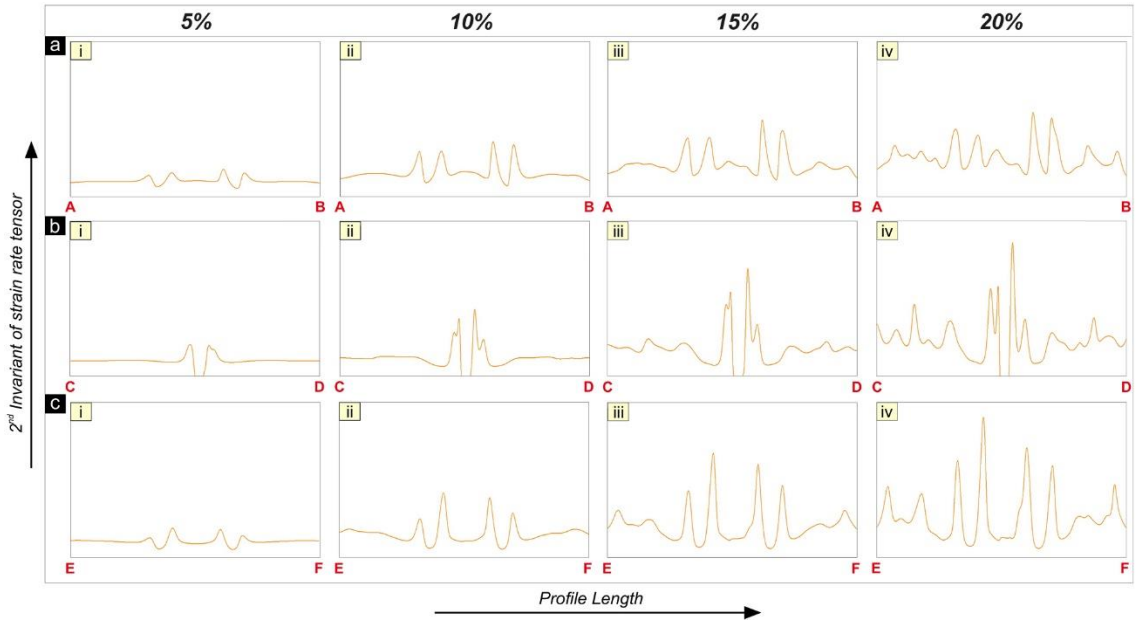

Figure S2: Across-band strain profiles in MS2 (locations of the profile lines: AB, CD, and EF, shown in Fig 6). Note that the strain profiles show multiple peaks signifying the formation of multiple shear bands in the core zone.

S3. Field study of natural shear zones

We studied a few centimetres to tens of metres long ductile shear zones in the Chotonagpur Granite Gneissic Complex (CGGC), focusing upon regions north of the South Purulia Shear Zone (SPSZ). The shear zones are associated with alkali granite, brecciated quartzite, apatite-magnetite bearing chert, U-Th mineral-bearing pegmatite and mafic-

ultramafic rocks. The host rock types include banded, porphyritic and augen granite gneisses, garnet-bearing quartzo-feldspathic gneisses, khondalite, amphibolites and mafic granulites, which generally contain penetrative tectonic foliations of single or multiple generations. The host foliations act as markers, showing sharp deflections across shear bands that allow us to identify the mode of shear localization. In places we could recognize mechanical heterogeneities as nucleating agents of shear zones. For example, high-temperature metamorphic rocks in the Jasidh area show band localization in the vicinity of quartzo-feldspathic aggregates, which possibly represent melt lenses (weak zones) produced by partial melting during the granulite facies metamorphism. This kind of field examples support our experimental interpretation that mechanically weak heterogeneities can be a crucial factor for the formation of isolated shear zones in continua.

We chose three prominent locations: 1) Bero Hillocks (23°32'09.5" N, 86°40'01.3" E) near Raghunathpur town, 2) Purulia-Asansol Road transect near Baraseni (23°25'20.9"N 86°28'48.8"E), and 3) Jasidih (24° 31′ 19.2″ N, 86° 38′ 51.72″ E) (Fig S1). Location 1 is predominantly composed of biotitic granite gneiss, which shows excellent shear band structures with thick strongly shear core, sometimes flanked by excellent drag zones on both sides, while some shows relatively weakly deformed matrix. Lithologically, Location 2 is a fine-granied granulite-facies rock, primarily composed of alkali-feldspar, with minor amounts of quartz, mica, garnet and tourmaline. Classically this rock type is also termed as Leptynite and they often show a planar gneissic structure. Location 2 exhibits extensive micro shear band structures with a cross cutting relationship throughout the exposure (Fig 8 a). Location 3 is situated near the Jasidih area, which lies in the northernmost part of CGGC. Lithologically, this area is predominantly of migmatitic felsic orthogneiss origin,

with random enclaves of meta -sedimentary and meta-mafic rocks. We found excellent shear bands occurring in the vicinity of elliptical to semi-elliptical heterogenous clasts (Fig 8b), that can be well correlated with our heterogenous models (Fig 2 b).

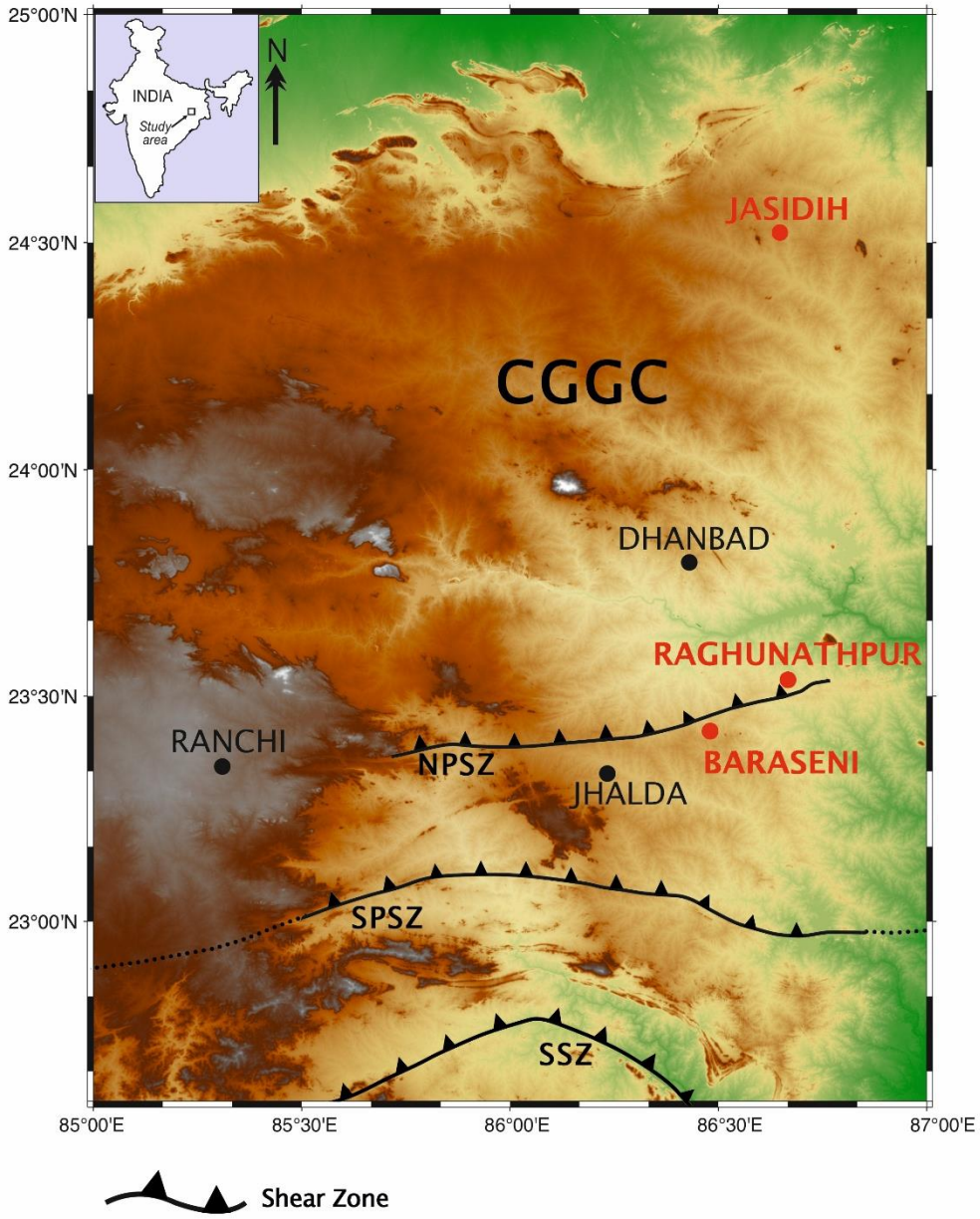

Figure S3: A simplified geological map of the East Indian Precambrian craton, showing the locations of the Singhbhum Shear Zone (SSZ), the South Purulia Shear Zone (SPSZ), the North Purulia Shear Zone (NPSZ) and the Chotanagpur Granite Gniess Complex (CGGC). Field areas are marked by red dots in the map.

S4. Strain profiles from field studies

This section presents the strain profiles obtained from strain analyses performed in field outcrops. Strain profiles were obtained by calculating the finite strain (ε) across various types of shear zones. Type I shear zones containing narrow shear bands observed in an area near Purulia town, showed a characteristic curve with a high peak showing large ε values implying intense shear localisation across the narrow shear bands (Fig 9b-i). Type II shear zones showed gradational shear strain variation from weakly deformed wall to highly sheared core forming a typical bell-shaped curve (Fig 9b-ii). On the contrary, Type III shear zones are characterized by a plateau like strain profile with very narrow gradational zone (Fig 9b-iii). This characteristic shape results due to formation of a very narrow drag zone on both sides of the homogenous core zone.

Table S1: Numerical Parameters and Their Values

Parameters	***Symbol***	***Natural Values***	***Numerical Input Values***
Model length	L	60 km	6
Model width	W	40 km	4
Model reference strain rate	$\dot{\gamma}_o$	$1.00e^{-15}$	1
Model reference density	ρ	2700 kg m^{-3}	1
Model reference viscosity	η_0	$1e^{20}$ Pas	1
Initial Cohesion	C_i	20 Mpa	0.08
Cohesion after Softening	C_s	5 Mpa	0.02
Angle of friction	ϕ	25° - 30°	25° - 30°
Maximum Yield stress	σ_{max}	1000 Mpa	3.7
Minimum Yield stress	σ_{min}	10 Mpa	0.04
Elastic shear module	G	5×10^9 Pa	18.5